Mid-Holocene to present-day evolution of the Indian monsoon in transient global simulations

Julien Crétat, Pascale Braconnot, Pascal Terray, Olivier Marti, Fabrizio Falasca

Mid-Holocene to present-day evolution of the Indian monsoon in transient global simulations

Julien Crétat[1,2,*], Pascale Braconnot[1], Pascal Terray[3], Olivier Marti[1] and Fabrizio Falasca[4]

1 IPSL/Laboratoire des Sciences du Climat et de l'Environnement, CEA-CNRS-UVSQ, Université Paris Saclay, Gif-sur-Yvette, France

2 Biogéosciences/CRC, CNRS-UB, Université de Bourgogne, Dijon, France

3 IPSL/Laboratoire d'océanographie et du climat : expérimentations et approches numériques, Sorbonne Universités-CNRS-IRD-MNHN, Université Paris 6, Paris, France

4 School of Earth and Atmospheric Sciences, Georgia Institute of Technology, Atlanta, GA 30332, USA

Submitted to Climate Dynamics

28/02/2020

Revised

04/06/2020

28/07/2020

* Now at Science Partners, Paris, France

Correspondance to julien.cretat@science-partners.com

Abstract

The low-frequency evolution of Indian rainfall mean-state and associated interannual-to-decadal variability is discussed for the last 6000 years from a multi-configuration ensemble of fully coupled global transient simulations. This period is marked by a shift of Indian Summer Monsoon Rainfall (ISMR) distribution towards drier conditions, including extremes, and a contraction of the rainy season. The drying is larger in simulations with higher horizontal resolution of the atmosphere and revised land surface hydrology. Vegetation-climate interactions and the way runoff is routed to ocean modulate the timing of the monsoon onset but have negligible effects on the evolution of seasonal rainfall amounts in our modeling framework in which carbon cycling is always active. This drying trend is accompanied by changes in ISMR interannual-to-decadal variability decreasing over north and south India but increasing over central India (20°-25°N).

The ISMR interannual-to-decadal variability is decomposed into six physically consistent regimes using a clustering technique to further characterize its changes and associated teleconnections. From 6 to 3.8 kyr BP, the century-to-century modulations in the frequency of occurrence associated to the regimes are asynchronous between the simulations. Orbitally-driven trends can only be detected for two regimes over the whole 6 kyr BP to 0 kyr BP period. These two regimes reflect increased influence of ENSO on both ISMR and Indian Ocean Dipole as the inter-hemispheric energy gradient weakens. Severe long-term droughts are also shown to be a combination of long-term drying and internally generated low-frequency modulations of the interannual-to-decadal variability.

Keywords: Holocene, Indian Summer Monsoon, internal variability, orbital forcing, rainfall mean-state and variability, transient simulations

1. Introduction

The Indian Summer Monsoon Rainfall (ISMR) provides about 80% of the annual rainfall amounts over India from June to September (JJAS) with significant variability on a wide range of timescales (Roxy and Chaithra 2018). Since ISMR variations profoundly impact on livelihood, which mostly relies on rain-fed agriculture (Kesava Rao et al. 2020), improved understanding of multi-scale ISMR variations is thus critical to reduce society vulnerability to climate change and extremes. Two ranges of natural variability, interannual and decadal timescales, are critical for adaptation planning and long-term mitigation.

At the interannual timescale, the El Niño Southern Oscillation (ENSO; Philander 1983) and the Indian Ocean Dipole (IOD; Saji et al. 1999) are the two main modes of ocean-atmosphere variability affecting ISMR. El Niño events are associated with an eastward shift of the Walker circulation in the Indo-Pacific sector, which induces subsidence and dry conditions over India, and *vice versa* during La Niñas (Walker 1924; Sikka 1980; Rasmusson and Carpenter 1983; Wang et al. 2005). Positive IODs are associated with warm sea surface temperature (SST) anomalies in the western tropical Indian Ocean (IO) and cold SST anomalies in the eastern equatorial IO coupled to low-level easterly wind anomalies along the equatorial IO. Positive IODs favor the existence of a reversed regional Hadley cell that enhances rainfall over India, and *vice versa* for negative IODs (Ashok et al. 2001, 2004; Gadgil et al. 2004; Ashok and Saji 2007). However, positive IODs are often triggered by El Niños and negative IODs by La Niñas (Behera et al. 2006). It is therefore nontrivial to disentangle the effects of both ENSO and IOD on ISMR from observations alone. At the decadal time scale, ISMR is modulated by the Pacific Decadal Oscillation (PDO; Mantua et al. 1997; Joshi and Kucharski 2017). A negative/positive phase of the PDO promotes wet/dry ISMR anomalies. Additionally, a further amplification of this link has been found when PDO and ENSO are in phase (Krishnan

et al. 2003; Roy et al. 2003; Krishnamurthy and Krishnamurthy 2013; Malik et al. 2017; Malik and Brönnimann 2018). Finally, the Atlantic Multidecadal Oscillation (Enfield et al. 2001) can also influence ISMR (e.g., Malik et al. 2017; Malik and Brönnimann 2018).

The extent to which low-frequency modes of variability modulate ISMR variability at interannual-to-decadal timescales is still an open question. The ISMR long-term fluctuations have been related to changes in solar radiations induced by changes in Earth's orbit. For example, mid- to late Holocene changes in orbital configuration weaken the inter-hemispheric energy gradient as well as land-sea and moist static energy contrasts (e.g., Kutzbach 1981; Joussaume et al. 1999). This leads to a decrease and southward shift of boreal summer monsoons in both observations (e.g., Bartlein et al. 2011) and models (e.g., Liu et al. 2003; Zhao et al. 2005; Braconnot et al. 2007a-b; Marzin and Braconnot 2009; Zhao and Harrison 2012; Harrison et al. 2015). Also, modeling studies have shown that the buildup of a seasonal IOD-like pattern in autumn contributes to delay the monsoon withdrawal during the mid-Holocene (Zhao et al. 2005; Braconnot et al. 2007).

Paleo reconstructions reveal that the mid- to late Holocene drying trend of ISMR is punctuated by long periods of anomalously high/low rainfall that are not necessarily phased in time across India (e.g., Kathayat et al. 2016, 2017; Kaushal et al. 2018; Kumar et al. 2019), as well as mega-droughts such as the 4.2 kyr BP event (Staubwasser et al. 2003; Giesche et al. 2019). These studies suggest that regional changes in ISMR can often result from the highly nontrivial interplay between internal variability and external forcing of the system.

Paleo-reconstruction archives are clues for characterizing and understanding past climates. However, their spatial coverage and temporal resolution remain often too low or inconstant

over time to easily address changes in the interannual-to-decadal ISMR variability and associated teleconnections during the Holocene. Transient global simulations run with general circulation models are thus complementary tools to investigate ISMR evolution. Until recently, such simulations were performed using accelerated changes in orbital forcing (Lorenz et al. 2004, 2006; Varma et al. 2012) because of huge computational constraints. This protocol does not allow us to examine the rhythm of changes nor interannual-to-decadal variability since orbital forcing is accelerated by a factor 10 to 100 (Varma et al. 2016). Long transient simulations performed with Earth System models and yearly-updated orbital forcing (Liu et al. 2009; Jungclaus 2011) offer new possibilities to overcome these limitations since they provide a thorough spatio-temporal continuum of climate evolution. Such simulations have been used successfully to discuss the evolution of the Asian and African monsoons during the Holocene (Dallmeyer et al. 2015, 2019; Shi and Yan 2019; Jalihal et al. 2019), their multi-scale changes and teleconnections (Braconnot et al. 2019a-b), or mega-drought during the 4.2 ka BP event (Yan and Liu 2019). They are also tailored for the investigation of the complex spatio-temporal interrelationships in the ENSO-IOD-ISMR system.

In this study, we build on the work of Braconnot et al. (2019b), who show that ISMR interannual-to-decadal variability increases from mid- to late Holocene due to increased ENSO variability in two 6000-yr transient simulations ran with the IPSL (Institut Pierre et Simon Laplace) Earth system model. Here, we consider a multi-configuration ensemble of transient simulations to refine their results. We investigate the effects of horizontal resolution, land hydrology, vegetation and runoff on changes in ISMR, with a focus on its seasonality at the monthly timescale and on its probability density function and extremes at the seasonal timescale. We also investigate changes in the interannual-to-decadal variability of ISMR and its teleconnections based on a clustering approach. Our aim is to highlight regional patterns in

ISMR interannual changes and to assess the temporal stability of ISMR teleconnections in the transient simulations. The results of these analyses should also provide guidance to design appropriate model-data comparison to analyze monsoon variability when dealing with a wide range of spatio-temporal timescales.

Section 2 describes the simulations and the methodology used. Section 3 gives an overview of trends in Indian rainfall seasonality, probability density function and extremes. Section 3 also analyzes the rhythm and spatial consistency of changes at the local scale over the Indian sector. Section 4 investigates changes in ISMR interannual-to-decadal variability and its teleconnections through the regime approach with a focus on 6–3.8 kyr BP and discusses the robustness of our results. Section 5 summarizes the results and gives the main conclusions.

2. Model simulations and methodology

2.1 The IPSL model

We consider two model versions of the IPSL Earth System model (Table 1). The first one, called TR5A hereafter, is the IPSL-CM5A model version used for the CMIP5 ensemble of past, present and future simulations (Dufresne et al. 2013; Mignot and Bony 2013) and modified by Sepulchre et al. (2019). TR5A couples atmosphere, land surface, ocean and sea-ice, and accounts for energy, water and carbon cycles. The second version, called TR6A hereafter, includes a new 11-layer hydrological model, a prognostic 3-layer snow model and the possibility to switch on a dynamical vegetation component (Braconnot et al. 2019a). In both model versions, the vegetation in each grid box is represented by 13 Plant Functional

Types (PFTs) and carbon cycle is interactive. The leaf area index (LAI) is thus fully interactive and varies depending on energy, water and carbon cycles regardless of the model version. When vegetation is prescribed, the 13 PFTs are assigned to a fixed land cover map. When vegetation is computed, only natural vegetation is accounted for and the distribution of the 13 PFTs in each model grid cell varies with time.

The resolution of the atmosphere is 3.75° x 1.875° for TR5A and 2.5° x 1.25° for TR6A on the horizontal and 39 levels for the two versions on the vertical. For ocean, TR5A and TR6A share the same 2° ORCA configuration (Madec et al. 2017), with a tri-polar grid, mesh refinement at the equator and 31 vertical levels. River and direct runoff are routed to the corresponding ocean coastal grid box. Specific schemes connect snow accumulation over the ice sheet and endorheic basins to the ocean (Marti et al. 2010) to ensure a perfect closure of the water cycle. The corresponding algorithm now uses a full parallel version of the interpolation weights between the land-atmosphere and ocean grids. The parameters of the new algorithm were chosen to produce similar results as before. This new version of the land-ocean runoff is called CM6 in Table 1.

2.2 Transient simulations

An ensemble of five transient simulations is performed with yearly changes in orbital parameters and trace gases following the protocol proposed by Otto-Bleisner et al. (2017). This ensemble accounts for differences in model resolution, the representation of land-surface hydrology, snow and river runoff, as well as dynamical vegetation. Details on major components of each simulation can be found in Table 1.

Two simulations, TR5AS-Vlr01 and TR6AV-Sr02 span the time range from 6 to 0 kyr BP (Braconnot et al. 2019a-b), with 0 kyr BP corresponding to 1950 Common Era. The remaining simulations also start at 6 kyr BP but are 4000-yr or 2250-yr long integrations (Table 1).

The TR5AS-Vlr01 is run with the TR5A model version and with vegetation prescribed to the IPSL-CM5A 1850 reference map (Dufresne et al. 2013). The other simulations are run with the TR6A model version. The TR6AV-Sr02 simulation has dynamical vegetation. The TR6AS-Sr10 and TR6AS-Sr12 simulations are similar to TR6AV-Sr02, except that vegetation is prescribed to the 1850 reference map for the former and to the mid-Holocene natural vegetation as computed by the model for the latter (Table 1). An error was found in the first release of the interpolation weights, which might affect the results of the TR6AV-Sr02, TR6AS-Sr10 and TR6AS-Sr12 simulations (Table 1). In these simulations, a fraction of the river and direct runoff is redistributed globally and not at the river mouth ("inter" in Table 1). This doesn't affect the water closure of the model, but the ocean regional circulation. A simulation similar to TR6AS-Sr10, called TR6AS-Sr11 (Table 1), was thus run to test the effect of this bug ("inter") compared to the CM6 land-ocean river runoff.

The different model versions and model setups produce slightly different mean climate and climate characteristics (Braconnot et al. 2019a). The initial state for each transient simulation results from a 1,000-yr long mid-Holocene simulation (i.e., with Earth's orbit and trace gases prescribed to mid-Holocene values and kept constant throughout the simulation) performed with the corresponding version of the model. The initial states are thus entirely consistent with the mid-Holocene climate simulated by each model configuration, ensuring no artificial model drift at the beginning of the transient simulations.

2.3 Statistical analysis of Indian rainfall and teleconnections

Complementary analyses allow us to characterize the long-term evolution of ISMR and of its variability. We first use a rainfall index area-averaged over India (land points within 5°-25°N and 77°-88°E) to assess changes in (i) the seasonality of the Indian rainfall mean-state and its variability at the monthly timescale, (ii) the probability density function of seasonal ISMR amounts during boreal summer (i.e., JJAS) and (iii) extreme ISMR years (i.e., flood and drought years). This domain embeds regions strongly affected by boreal summer Indian monsoon. Analyses are performed considering 100-yr adjacent windows from 6 kyr BP onwards. Rainfall mean-state is defined as the average within each 100-yr window, while rainfall variability is defined either as the standard-deviation within each window or as anomalies with respect to the mean-state estimated in the window. The 100-yr length of the windows is retained to focus on interannual-to-decadal variability. The century-to-century evolution of these descriptors will be interpreted as centennial-to-multicentennial modulation of rainfall mean-state and interannual-to-decadal variability.

To account for potential spatial disparity in the ISMR evolution that are hidden in the area-averaged index, we then adopt a “regime” approach based on the Agglomerative Hierarchical Clustering (AHC; Gong and Richman 1995). This technique, presented in Appendix A, is retained to detect recurrent anomalous rainfall patterns over India at the interannual-to-decadal timescale. It is preferred to Empirical Orthogonal Function analysis because it allows us to highlight regional nuances without imposing artificial north–south or west–east structures induced by orthogonality relationships and to account for nonlinearities in the teleconnection between (wet and dry) ISMR regimes and ENSO.

For the AHC analyses, anomalies of JJAS rainfall patterns are computed for each adjacent 100-yr window as the departures from the corresponding rainfall mean-state inside the window. The AHC is fed by the 5 simulations simultaneously to focus on the shared signals across the simulations. The AHC provides a hierarchy of clusters from N to 1, with N being the total number of classified (time) patterns. The patterns are grouped based on their similarity and to minimize intra-cluster variance and maximize inter-cluster variance. The optimal number of ISMR regimes (i.e., clusters) is a compromise between the intra- and inter-cluster variance and the physical meaning of the identified clusters. Here, we detect 6 ISMR regimes using different metrics (see Appendix A for details). The 6 ISMR regimes are then characterized by computing their center of gravity, that is, by averaging all anomalous patterns in JJAS rainfall, diverse atmospheric fields and SST belonging to each regime. Their robustness is assessed through statistics to test whether or not the centers of gravity of the regimes differ significantly from the center of gravity of the whole population (Student t-test at the 95% confidence level) and by discussing the similarity between them and those associated to each simulation (e.g., the center of gravity of all patterns of TR5AS-Vlr01 belonging to regime #1).

2.4 Representation of the Indian monsoon by the IPSL model

The two model versions reasonably capture the mid-Holocene wetting of the Northern Hemisphere monsoon regions (Kageyama et al. 2013a-b; Braconnot et al. 2019a) and the teleconnection between the Indian monsoon and ENSO at the interannual timescale during the recent period (Braconnot et al. 2019b). Here, their ability in capturing both the mean-state and interannual-to-decadal variability of Indian rainfall is assessed for modern conditions against

three observational monthly products: the All Indian Rainfall index (AIR; Parthasarathy et al. 1995), which is an area-weighted average of 306 rain gauges distributed across India from 1871 onwards, and the GPCP version 2.2 (Adler et al. 2003) and CRU-TS4.01 (Harris et al. 2014) data.

Regarding rainfall mean-state, the magnitude of the monsoon peak and JJAS amounts is close to observations in TR6AV-Sr02, while depicts a ~2 mm/day dry bias in TR5AS-Vlr01 (Fig. 1a and Table 2). The latter dry bias is typical of low-resolution global coupled simulations (Sperber et al. 2013; Goswami and Goswami 2017; Terray et al. 2018). The improvement of TR6AV-Sr02 on TR5AS-Vlr01 is due to a better penetration of the monsoon flow along the Himalaya foothill induced by increased horizontal resolution (Fig. 2) and to increased local recycling induced by the 11-layer hydrology model (Braconnot et al. 2019a). On the other hand, horizontal resolution and hydrology do not affect the onset and demise phases of the Indian monsoon, which are similar between the two model's versions. The fast withdrawal observed between September and October is accurately captured, while the onset observed in June is delayed by 1 month in the simulations (Fig. 1a). The 1-month delay in the onset results from a too slow northwestward propagation of the rain belt during early summer over India (Fig. 2). This slow propagation involves a too late inversion of the meridional tropospheric temperature gradient between landmass and the IO due to a persistent cold bias over the Himalayas (Marzin and Braconnot 2009) and Indo-Pacific SST biases intrinsic to ocean-atmosphere coupled simulations (Sperber et al. 2013; Prodhomme et al. 2015). Note, however, that the northernmost extent of the monsoon in August and September is consistent with observations (Fig. 2).

Regarding rainfall variability, the observations depict a plateau of 1.5 $mm.day^{-1}$ from June to

September when considering the standard-deviation of the long time series in the AIR and CRU data (Fig. 1b). This plateau hides large observed variability of the monsoon onset and demise when considering 20-yr long time series (see GPCP and thin curves for AIR in Fig. 1b). This double peak is captured by the two simulations despite a clear 1-month delay of the first peak linked to the aforementioned bias in the mean-state and exaggerated magnitude, especially in the TR6AV-Sr02 (Fig. 1b and Table 2, second column).

3. Trends in seasonality and boreal summer Indian monsoon rainfall

3.1 Evolution of Indian rainfall seasonality

The evolution of Indian rainfall seasonality, estimated in 100-yr adjacent windows, is affected by the insolation and trace gas forcing (Fig. 3). The TR5AS-Vlr01 and TR6AV-Sr02 depict decreased monthly rainfall amounts throughout the seasonal cycle and reduced length of the Indian monsoon season from mid- to late Holocene (Fig. 3a-b), with delayed onset and early withdrawal. The delayed onset is not affected by the calendar effect induced by changes in orbital forcing in early boreal summer when the vernal equinox is set to March 21 in all simulations (Joussaume and Braconnot 1997; Bartlein and Shafer 2019). Daily output would be required to fully assess the calendar effect on the early withdrawal since this effect is maximal in late boreal summer with the calendar reference used here. However, the reduced length of the Indian monsoon is consistent with Marzin and Braconnot (2009). These authors analyzed daily values and suggested that the gradual warming of the tropical ocean and cooling of the Northern Hemisphere late summer SST throughout the Holocene are the main drivers of the reduced length of the Indian monsoon from mid- to late Holocene. Despite the

drying trend in rainfall mean-state (Fig. 3a-b), TR5AS-Vlr01 and TR6AV-Sr02 simulate increased interannual-to-decadal variability with time, in June-July for TR5AS-Vlr01, but for all monsoon months in TR6AV-Sr02 (Fig. 3c-d). The opposite trends between rainfall mean-state and rainfall variability highlight the need to carefully untangle mean-state and variability evolutions in climate change studies.

The broad features of rainfall mean-state seasonality of the other simulations are close to TR6AV-Sr02. It is, however, worth noting that vegetation-climate feedbacks and the way river runoff is routed to ocean have significant impacts on the onset and early part of the Indian monsoon (Fig. 3e-h). These results are consistent with the sensitivity experiments of Sooraj et al. (2019), who have demonstrated that albedo perturbations play a significant role on the Indian monsoon during the first part of the rainy season (e.g. June-July), while convective processes dominate ISMR afterward. The simulation with "inter" river runoff (TR6AS-Sr10: Fig. 3e) is much wetter in June-July than the simulation with CM6 runoff (TR6AS-Sr11: Fig. 3f). In addition, the simulation with prescribed 1850 vegetation (TR6AS-Sr10: Fig. 3e) is wetter in June and drier in July than the simulations with prescribed mid-Holocene vegetation (TR6AS-Sr12: Fig. 3g) or dynamical vegetation (TR6AV-Sr02: Fig. 3h). Finally, the use of a fixed vegetation map in TR6AS-Sr12 induces a significant shift of ISMR from the second half to the first part of the rainy season from 6 to 3.8 kyr BP (Fig. 3e), but this specific time evolution is not simulated with a dynamical vegetation in TR6AV-Sr02. A dedicated study is needed to understand the mechanisms by which vegetation-climate feedbacks and river runoff affect the Indian monsoon onset. The interannual-to-decadal variability remains very noisy from one TR6A simulation to another from 6 to 3.8 kyr BP (not shown), highlighting the chaotic nature of this range of variability.

338 3.2 Pace of change in Indian summer monsoon rainfall

339

340 We now consider JJAS seasonal averages to assess the pace and magnitude of changes in
341 rainfall mean-state and variability during the Holocene. The JJAS season is chosen to
342 encompass differences in Indian rainfall amounts arising from changes in both the amplitude
343 and length of the monsoon with time. The Probability Density Function (PDF) of JJAS
344 rainfall amounts shifts towards lower values from mid- to late Holocene in the two 6000-yr
345 long simulations (Fig. 4a-b). While the shape of the PDF barely varies along the period in the
346 TR5AS-Vlr01 (Fig. 4a), it flattens and is more skewed to the left towards present-day
347 conditions in TR6AV-Sr02 (Fig. 4b). This reflects stronger changes in ISMR interannual-to-
348 decadal variability in the TR6AV-Sr02 than the TR5AS-Vlr01.

349

350 Both experiments simulate changes that are more significant for the 10% driest than 10%
351 wettest seasons estimated through a percentile approach (Fig. 4c). This confirms that the
352 drying concerns not only the center of the distribution, but also the drought years, which
353 become more severe towards present-day climate, especially in TR6AV-Sr02. The evolution
354 in the number of extreme ISMR seasons in each simulation (and not on each 100-yr window
355 extracted from the simulations) highlights that the drying trend in ISMR mean-state results
356 also from increased occurrence of droughts (Fig. 4d) rather than decreased occurrence of
357 floods (Fig. 4e). This result is very robust across the 5 simulations and is thus interpreted as a
358 response to orbital forcing. Note that the magnitude of changes is weaker in TR5AS-Vlr01
359 than the other simulations, especially after 4 kyr BP (Fig. 4d).

360

361 The evolution in the intensity and, to a greater extent, frequency of the driest and wettest JJAS
362 seasons depicts large inter-centennial fluctuations (Fig. 4c-e). The most striking example is

363 the evolution of the 10% driest ISMR seasons with up to 500 consecutive years depicting
364 increase or decrease in their occurrence (Fig. 4d). Associated changes exceed, by far, the
365 magnitude of the trend simulated for the last 6000 years. Such events are independent from
366 orbital forcing since they are not synchronized between the simulations and occur at any time
367 during the last 6000 years (Braconnot et al. 2019b).
368
369 3.3 Broader context of boreal summer changes
370
371 The broader context of JJAS changes in 100-yr mean-state and associated interannual-to-
372 decadal variability is now analyzed in the framework of Indo-Pacific rainfall and SST patterns
373 to provide a more comprehensive view of ISMR changes (Figs. 5-6). We focus the discussion
374 on the aspects that emerge in all simulations but show the results only for the TR6AV-Sr02
375 from 6 to 0 kyr BP.
376
377 Compared to 6-5.9 kyr BP, significant dry rainfall anomalies emerge over the Himalayas, and
378 immediately east of the western Ghats as soon as 5.9-5.5 kyr BP. They rapidly expand over
379 all India and grow in intensity afterwards (Fig. 5; contours). This drying reflects the direct
380 response of the Indian monsoon to the orbitally-driven weakening (strengthening) of
381 seasonality in the Northern (Southern) Hemisphere (Braconnot et al. 2007a). It is associated
382 to progressive SST cooling in most regions of the Northern Hemisphere and SST warming in
383 the Southern Hemisphere (Fig. 6; contours). Over the IO, anomalous SSTs reflect a
384 combination of these orbitally-driven global forcing and of changes in monsoon circulation
385 (Zhao et al. 2005). The negative rainfall anomalies trend over the IO between the Equator and
386 8°N (Fig. 5) is a key feature that emerges also in coral-based reconstructions (Abram et al.
387 2007) and is coupled to a shift towards negative IOD conditions in simulated SST patterns

(Fig. 6).

The pattern of changes in rainfall variability (Fig. 5; shadings) is well correlated to the pattern of changes in rainfall mean-state (Fig. 5; contours). Regions experiencing a drying trend are characterized by decreased variability, and *vice versa*. The only exception is central India (between 20°N and 25°N) where rainfall mean-state decreases but rainfall variability starts increasing after 3 kyr BP and keeps increasing until late Holocene (Fig. 5; shadings). The increased rainfall variability over central India is embedded in a pattern extending from the northeastern part of the Arabian Sea to the Bay of Bengal. This suggests a coherent large-scale amplitude variation of the monsoon trough over land and ocean in the IO region. Moisture convergence into central India and the monsoon trough becomes thus more variable with time. This also indicates that the increased variability of area-averaged Indian rainfall discussed in Braconnot et al. (2019b) reflects the behavior of central India.

Contrary to rainfall, the pattern of changes in SST variability (Fig. 6; shadings) does not resemble that of changes in SST mean-state (Fig. 6; contours). For the mean-state, the main tropical features in the simulations are the emergence of a well-defined cold tongue along the Equator in the eastern Pacific and eastern Atlantic and of a negative IOD-like SST pattern in the IO. Consistent with these mean-state changes and slow adjustments by ocean dynamics, SST variability increases in the central-to-eastern equatorial Pacific (e.g. enhanced ENSO variability) and the eastern equatorial Atlantic, but decreases in the eastern equatorial IO (off Java). Interestingly, the SST variability is enhanced in the western tropical IO, despite the decreased SST variability in the eastern tropical IO. This suggests that IOD modulations are not the main trigger of these changes of variability over the western IO. To sum up, these mid- to late Holocene changes of tropical SST are consistent with the amplification (cooling)

of the Pacific and Atlantic upwelling (Braconnot et al. 2012), increased ENSO variability reported during the Holocene (Emile-Geay et al. 2016) and a strong control of ENSO on tropical IO SST variability, especially the western IO, as seen in present-day climate (Crétat et al. 2017).

4. Changes in recurrent ISMR regimes and teleconnections

We now go one step further by analyzing ISMR interannual-to-decadal variability no more as a standard-deviation around the mean-state but through six recurrent ISMR regimes extracted from a cluster analysis of Indian rainfall anomalies with respect to the mean-state estimated in 100-yr windows (see Appendix A for details). The ISMR regimes are mainly discussed from 6 to 3.8 kyr BP within the 5-simulation ensemble to account for uncertainties induced by the model versions and setups. They are also briefly discussed for late Holocene and from mid- to late Holocene within the two 6000-yr long simulations to assess model skill and long-term trends in rainfall interannual-to-decadal variability, respectively.

4.1 Ensemble mean

Regimes #1 and #6 represent respectively ~14% and ~26% of the JJAS anomalous Indian rainfall patterns classified from 6 to 3.8 kyr BP (Table 3; 1st column). They both describe a weak meridional dipole in rainfall anomalies over India (Fig. 7a,f) associated with modest SST anomalies in the tropics (Fig. 8a,f). Regime #1 consists in significant wet and dry rainfall anomalies in central and south India, respectively (Fig. 7a). Regime #6 depicts a similar dipole structure but slightly shifted northward 6 (Fig. 7f: wet/dry anomalies north/south of ~15°N). Regime #1 is associated with warm tropical Pacific SST anomalies and cold North

438 subtropical SST anomalies in the three basins (Fig. 8a). This weakens the meridional
439 temperature gradient, hence limiting westerly wind anomalies over the Arabian Sea (Fig. 9a).
440 On the other hand, the increased meridional temperature gradient in regime #6 strengthens
441 westerly wind anomalies over Africa and North Africa and favors a northwestward shift of the
442 monsoon trough over India (Figs. 8f and 9f). Interestingly, the whole circulation pattern of
443 regime #6 is very similar to the one obtained by reducing the albedo over Sahara and Pakistan
444 arid regions in sensitivity coupled experiments (Sooraj et al. 2019).
445
446 The four remaining ISMR regimes are all associated with strong rainfall anomalies (Fig. 7b-
447 e), ENSO-like SST anomalies over the tropical Pacific (Fig. 8b-e) and significant modulations
448 of the monsoon circulation in the Indian sector (Fig. 9b-e). Despite weaker tropical Pacific
449 variability in mid- rather than late Holocene (Emile-Geay et al. 2016; White et al. 2018; Chen
450 et al. 2019), tropical Pacific SST variability remains the main driver of ISMR variability
451 during the mid-Holocene in our 5-simulation ensemble. Regimes #2 and #3 both represent
452 ~15% of the classified patterns from 6 to 3.8 kyr BP (Table 3; 1st column). They describe
453 significant wet anomalies over most or all India during La Niña-like conditions (Figs. 7b-c
454 and 8b-c). These wet anomalies are due to moisture convergence favored by significant
455 easterly wind anomalies over the western Pacific and eastern IO and an anticyclonic center
456 over the Bay of Bengal (Fig. 9b-c). However, regime #3 only is associated with a clear Gill-
457 type response to convection and latent heat release over India, with strengthened 850-hPa
458 southwesterlies over the Arabian Sea (Fig. 9c). On the other hand, regimes #4 and #5 (20%
459 and 10% of the classified patterns, respectively: Table 3; 1st column) describe either
460 widespread dryness or a north-south dipole over India under El Niño-like conditions (Figs.
461 7d-e and 8d-e). These abnormally dry conditions are systematically associated with 850-hPa
462 westerly wind anomalies over the eastern IO–western Pacific (north of 10°N), reduced

southwesterly monsoon fluxes over the Arabian Sea and a split of the monsoon trough over India (Fig. 9d-e), which is typical of drought conditions during the monsoon (Terray et al. 2005).

Interestingly, the two ISMR regimes associated with widespread wet/dry rainfall anomalies of same sign over all India (i.e., regimes #3 and #4: Fig. 7c-d) occur under well-defined ENSO-like – IOD collocation (Fig. 8c-d). Wet conditions over all India (Fig. 7c) are favored when these two coupled modes of variability collocate during their negative phases (i.e., La Niña-like and negative IOD: Fig. 8c). The reverse prevails for regime #4 (Figs. 7d and 8d). Regimes #3 and #4 reflect the strong control of ENSO-like variability on both IOD and ISMR variability during mid-Holocene. This does not preclude positive/negative IODs to promote wet/dry ISMR at times, as suggested by e.g. Ashok et al. (2001 and 2004) but this is clearly not the dominant signal found here at the interannual-to-decadal timescale.

To verify whether or not these results are consistent with regimes obtained for modern ISMR variability, the clustering has been applied to the last 100 years of the TR5AS-Vlr01 and TR6AV-Sr02 ensemble (i.e., 1851-1950) and to 1901-2016 observations (CRU data for rainfall and HadISST data [Rayner et al. 2003] for SST). Despite the 6 ISMR regime patterns simulated for the last 100 years are not strictly similar to those derived from 6 to 3.8 kyr BP, the main modes affecting ISMR variability persist (Fig. 10). This demonstrates that ENSO remains the main driver of interannual-to-decadal ISMR variability for the last 6000 years regardless of the strength of orbital and trace gas forcing. The comparison with CRU-HadISST data reveals that the simulations reasonably represent the observed ISMR regimes and associated teleconnections, despite distorted ENSO patterns and exaggerated coupling with IO and Atlantic SST variability. The only exception concerns the wet ISMR regime

associated to the strong IO basin-wide warming following strong El Niños (especially the 1982-83 and 1997/98) and the fast El Niño to La Niña transitions (Fig. 10), which represent the "best conditions" for a strong monsoon during recent decades (Boschat et al. 2011, 2012). The fact that this mode is not emerging in the simulations is probably linked to the inability of the model to produce a realistic negative IO feedback on ENSO, a bias shared by many current climate models, especially those with a significant cold tongue bias in the equatorial Pacific like the IPSL model (Kug and Ham 2012; Li et al. 2019; Terray et al. 2020).

4.2 Model version dependency

The model-version dependency of ISMR regimes is assessed in terms of anomalous rainfall patterns (Fig. 11) and total number of regime occurrence (Table 3). These analyses confirm that TR5AS-Vlr01 is an outlier, with largest departure from the ensemble mean (Fig. 11a) and underestimated occurrence of regimes #3 and #5 (Table 3). This suggests that ENSO and its teleconnection with ISMR and IO are much less diverse in this simulation compared to the others.

Overall, the ISMR regimes are very similar between the four TR6A simulations in terms of mean rainfall anomalies (Fig. 11b-e) and population (Table 3). We note, however, that the simulation set with fixed 1850 vegetation map (i.e., TR6AS-Sr10: Fig. 11b) deviates slightly more from the ensemble mean than those set with fixed mid-Holocene vegetation (i.e., TR6AS-Sr12: Fig. 11d) or dynamical vegetation (i.e., TR6AV-Sr02: Fig. 11e). Braconnot et al. (2019a) showed that bare soil and grass increase over India from mid- to late Holocene at the expense of forest (see their Fig. 10). Imposing more bare soil and grass and less forest over India during the mid-Holocene in TR6AS-Sr10 compared to TR6AS-Sr12 and TR6AV-

Sr02 may thus affect vegetation-climate feedbacks through the modulation of albedo and local recycling.

4.3 Evolution of the ISMR regimes and associated teleconnections

The frequency of occurrence of the ISMR regimes, computed every adjacent 100-yr windows, is marked by stochastic centennial-to-multi-centennial fluctuations (Fig. 12). Cross-correlations between each ISMR regime are very noisy regardless of the metric. In particular, the frequency of occurrence of regime #3 is poorly correlated with that of regime #4 ($r\sim=|0.1|$ in most simulations). This indicates that centuries with changes in the occurrence of wet rainfall anomalies associated with La Niña-like – IOD- collocation are not necessarily accompanied by changes in the occurrence of dry anomalies associated to El Niño-like – IOD+ collocation. These results are consistent with the trends for ISMR wet and dry years displayed in Fig. 4d-e.

On the other, none of the ISMR regimes depict a clear orbitally-driven trend from 6 to 3.8 kyr BP shared by the five simulations (Fig. 12). This contrasts with boreal summer SST variability in the Niño3.4, western tropical IO and eastern equatorial IO, which increases for the two former regions and decreases for the latter region in most simulations (Fig. 13a-c). The variability of the IOD, however, does not depict significant change (Fig. 13d) from 6 to 3.8 kyr BP. A first explanation of the absence of orbitally-driven changes in the ISMR regimes from 6 to 3.8 kyr BP could involve interferences with low-frequency modes of internal variability. However, this hypothesis is rejected since the AHC procedure applied to 2-20-yr filtered rainfall anomalies leads to similar results. Another explanation could be that 6–3.8 kyr BP changes in ENSO-like variability may be too weak to influence ISMR regimes

or, alternatively, that IOD variability may counteract ENSO's effects on ISMR, as suggested for the historical period (Ashok and Saji 2007).

When considering the last 6000 years, the ISMR regimes strongly connected to ENSO-like – IOD collocation become significantly more frequent from mid- to late Holocene in TR6AV-Sr02 (Fig. 14). This trend concerns both wet and dry regimes associated to ENSO – IOD collocation in their negative and positive phases, respectively (Fig. 14), while only the dry regime associated to El Niño-like – IOD+ collocation in TR5AS-Vlr01 (not shown). We thus make the hypothesis that the 6–3.8 kyr BP period is too short to detect changes in rainfall interannual-to-decadal variability, but that other variables could be better precursors of its long-term changes.

We thus examined changes in climate anomalies associated to the two ISMR regimes linked to ENSO – IOD collocation between the first and second half of the 6–3.8 kyr BP period (Fig. 15). In both cases, we identified modest but significant changes in precipitable water over India linked to changes in both local evaporation and moisture advection from the western IO and southeast Asia. These changes are associated with strengthened tropical SST anomalies, particularly over the Pacific under El Niño conditions, suggesting increased control of ENSO on the Indian monsoon thermodynamics from 6 to 3.8 kyr BP. Precipitable water is thus a good precursor of changes in the interannual-to-decadal variability of the water cycle due to the Clausius-Clapeyron relationship.

5. Discussion and conclusion

Results of the five transient simulations with the IPSL model show that the last 6000 years are marked by a significant drying trend in ISMR, consistent with previous studies (e.g., Bartlein et al. 2011; Dallmeyer et al. 2015; Braconnot et al. 2019b). This drying trend affects the whole ISMR distribution, including the intensity and number of the 10% driest and 10% wettest seasons and is associated to a contraction of the ISMR season (Figs. 3-4). The magnitude of the drying trend is larger in simulations set with higher resolution and the new surface hydrology. Both the way runoff is routed to ocean and vegetation-climate feedbacks modulate the onset phase of the Indian monsoon (Fig. 3), but have modest effects at the seasonal timescale, including the time evolution of the number and intensity in flood and drought years (Fig. 4).

The interannual-to-decadal variability of JJAS rainfall significantly decreases over most of India from mid- to late Holocene but increases over central India and adjacent oceanic regions (Fig. 5). This variability is then decomposed into 6 physically consistent rainfall regimes to investigate changes in the ISMR teleconnections.

- From 6 to 3.8 kyr BP, the regimes are very similar between the 4 TR6A simulations but depict less diversity in the TR5A simulation (Table 3). In all simulations, the two most energetic regimes in terms of rainfall intensity describe widespread dry/wet rainfall anomalies over India when ENSO and IOD collocate in their positive/negative phase (Figs. 7-8). This suggests that the ENSO forcing is dominant on both ISMR and IOD. The century-to-century frequency of occurrence of these two regimes is poorly correlated (Fig. 12), indicating that the relationship between ISMR and the two phases of ENSO-like – IOD is strongly skewed from 6 to 3.8 kyr BP at the centennial timescale. Furthermore, the frequency of occurrence of these two ISMR regimes does not change from 6 to 3.8 kyr BP, contrary to the intensity of precipitable water (Fig. 15) identified as a good parameter to detect emerging trends in

588 monsoon variability. Rainfall appears to be the last link in the chain and is mediated by
589 dynamic changes, which may have different and remote origins. This leads us to conclude that
590 a threshold needs to be reached prior to see significant trends in rainfall interannual-to-
591 decadal variability.

592 • From 6 to 0 kyr BP, these two ISMR regimes become more frequent from 6 to 0 kyr
593 BP (Fig. 14) as ENSO amplitude strengthens in our modeling framework (Fig. 6), consistent
594 with increased ENSO variability as inferred by paleo reconstructions (Cobb et al. 2013; Carré
595 et al. 2014; Emile-Geay et al. 2016). This suggests a reorganization of ISMR (and IOD)
596 interannual-to-decadal variability from mid- to late Holocene, with increasing influence of
597 ENSO and associated changes in the Walker circulation on both ISMR and IOD. On the other
598 hand, the slow evolution of interannual-to-decadal variability of JJAS Indian rainfall is never
599 linked to IOD only in our modeling framework, consistent with ENSO-removed experiments
600 (Crétat et al. 2017). This does not preclude the existence of IOD forcing on the Indian
601 monsoon in some specific years or periods when ENSO is at rest. It would be worth to
602 examine the ISMR–IOD relationship at different timescales and for different time slices with
603 partially coupled simulations (e.g. without ENSO) to refine these results.

604

605 We also highlight that ISMR mean-state and interannual-to-decadal variability exhibit
606 significant modulations at the multidecadal-to-multicentennial timescales that are not
607 synchronous between the simulations (Figs. 4 and 12). This is consistent with previous
608 modeling findings (e.g., Dalmeyer et al. 2015) and paleo reconstructions over India (Kathayat
609 et al. 2016; Kaushal et al. 2018). Long-term droughts such as the multidecadal-to-centennial
610 4.2 kyr BP event (Lézine et al. 2017; Yan and Liu 2019) may thus be caused by internal
611 variability since solar cycles are not imposed in our simulations. Understanding their
612 triggering mechanisms would lead to a strong improvement of ISMR predictability.

Finally, this study provides interesting tracks to model-data comparisons in the Indian sector. Mean-state and variability should be examined separately since their evolution can be opposite from mid- to late Holocene and their forcing mechanisms may differ. This also stands for the IO, which displays a positive-to-negative IOD-like SST mean-state, but increased (decreased) interannual-to-decadal variability in its western tropical (eastern equatorial) part from mid- to late Holocene (Fig. 6). Our results strongly suggest that this enhanced SST variability in the western IO is remotely forced by ENSO changes, independently of IOD or local mean-state changes. This complexity among timescales requires more investigations and may explain the disagreement among paleo-proxies for IOD evolution (Kwiatkowski et al. 2015 versus Abram et al. 2007). Diagnosing changes or specific events in paleoclimate records remains, however, a great challenge since there is only a small probability for "big events" resulting from multiscale forcing and internal variability to be synchronous between paleo-reconstructions and simulations. Strategies based on analog are thus necessary to foster model-data comparisons and to utilize models for assessing the mechanisms driving such compound events.

Appendix A: AHC procedure

In this study, the AHC is adopted to identify recurrent ISMR regimes within our multi-configuration ensemble and analyze their temporal evolution primarily from 6 to 3.8 kyr BP but also from 6 to 0 kyr BP and for the 1851-1950 period. The AHC procedure consists in merging *N* anomalous JJAS rainfall patterns into *N*-to-1 clusters of size 1-to-*N* according to their spatial similarity. The similarity between all pairs of patterns is measured using the Euclidean distance. Each pattern is merged with another according to the smallest pairwise Euclidean distance. The resulting merged cluster is then paired with another pattern or another cluster according to the Ward algorithm (Ward 1963), which minimizes intra-cluster variance and maximizes inter-cluster variance at each merging step. The procedure continues until all patterns are merged in a unique cluster. For a more detailed explanation of the AHC procedure we refer the reader to Crétat et al. (2019).

The AHC is applied to a time-space matrix constructed in three successive steps. Anomalous JJAS rainfall patterns are computed over India (i.e., 58 land points within 5°-25°N and 77°-88°E) for each simulation and each of the 22 100-yr windows from 6 to 3.8 kyr BP. For each 100-yr window, the 100 anomalous rainfall patterns are defined as the departure from the corresponding 100-yr rainfall mean-state pattern. The anomalous rainfall patterns from the TR5AS-Vlr01 simulation are interpolated onto the horizontal resolution of the TR6A simulations (see Table 1) using a bilinear algorithm. The anomalous patterns from the five simulations are concatenated in a time-space matrix. A total of 10980 patterns are classified from 6 to 3.8 kyr BP instead of 11000 (2200 JJAS seasons x 5 simulations) because two simulations, TR6AS-Sr10 and TR6AS-Sr12, have 10 years missing due to technical issues with the data storage. The same methodology is applied from 6 to 0 kyr BP and for the 1851-

654 1950 periods for the ensemble of the two 6000-yr simulations.

655

656 Figure A1 shows the dendrogram tree obtained at the end of the AHC procedure applied to
657 the 5-simulation ensemble from 6 to 3.8 kyr BP. The dendrogram summarizes all merging
658 from N to 1 clusters of size 1 to N (with N=10980 being the total number of anomalous
659 rainfall patterns feeding the AHC), as well as the evolution of the similarity metric for the last
660 10 merging. The evolution of the similarity metric indicates three main abrupt jumps: from 6
661 to 5 clusters, from 3 to 2 clusters and from 2 to 1 clusters. A 2-cluster cutoff would mix ISMR
662 regimes with opposite rainfall and SST anomalies (compare regimes #1 and #6 in Figs. 7-8).
663 A 3-cluster cutoff would also mix very different regimes (compare regimes #1 with regimes
664 #2-3 in Figs. 7-8) and would merge regimes related to ENSO-like conditions with regimes
665 related to ENSO-like – IOD collocation (compare regimes #2 and #3 and regimes #4 and #5
666 in Fig. 8). Here, we retain a 6-cluster cutoff to avoid such a mixing, which has no physical
667 consistency, and because we aim at discussing internal variability and orbitally-forced
668 evolution of only physically consistent regimes. This high-degree of refinement is required
669 here since changes in ISMR variability remain subtle from mid- to late Holocene (Braconnot
670 et al. 2019b).

671

672 The statistical robustness of a 6-regime cutoff is assessed by examining the spatial correlation
673 between each anomalous rainfall pattern within a regime and its center of gravity defined as
674 the ensemble mean anomalous rainfall pattern of the regime. When this spatial correlation is
675 below 0.2, the patterns are considered as outliers. The 0.2 threshold is deliberately low to
676 avoid excluding patterns which are close to the center of gravity but slightly shifted in space.
677 About 20% of outliers are detected. They are almost equally distributed within the five
678 simulations. These outliers are removed from all the analyses. Once the outliers removed, the

679 6 ISMR regimes synthesize 8963 patterns. The spatial correlation values obtained between
680 each pattern and its corresponding outlier-free center of gravity exceed +0.35 more than 75%
681 of the time and the median correlation reaches at least +0.5 whatever the regime.

Acknowledgments

We acknowledge PRACE for awarding us access to Curie at GENCI@CEA, France (THROL project) to start the simulations. The simulations were also performed using HPC resources from GENCI-TGCC thanks to a high-end computing access grant and to our annual allocation time (gen2212). This work is supported by the JPI-Belmont PACMEDY project (ANR-15-JCLI-0003-01). It benefits from the development of the common modeling IPSL infrastructure coordinated by the IPSL climate modeling center (https://cmc.ipsl.fr/). We also acknowledge the three anonymous reviewers for their constructive comments.

692 **References**

693

694 Abram N, M Gagan, Z Liu, et al. (2007) Seasonal characteristics of the Indian Ocean Dipole
695 during the Holocene epoch. Nature 445:299–302
696 Adler RF, et al. (2003) The Version 2 Global Precipitation Climatology Project (GPCP)
697 Monthly Precipitation Analysis (1979 - Present). J Hydrometeor 4(6):1147–1167
698 Ashok K, Z Guan, T Yamagata (2001) Impact of the Indian Ocean dipole on the relationship
699 between the Indian monsoon rainfall and ENSO. Geophys Res Lett 26:4499–4502
700 Ashok K, Z Guan, NH Saji, T Yamagata (2004) Individual and combined influences of ENSO
701 and the Indian Ocean dipole on the Indian summer monsoon. J Clim 17:3141–3155
702 Ashok K, NH Saji (2007) On impacts of ENSO and Indian Ocean dipole events on the sub-
703 regional Indian summer monsoon rainfall. Nat Hazards 42-2:273–285
704 Atsawawaranunt K, L Comas-Bru, S Amirnezhad Mozhdehi, et al. (2018) The SISAL
705 database: a global resource to document oxygen and carbon isotope records from
706 speleothems. Earth Syst Sci Data 10:1687–1713
707 Bartlein PJ, SP Harrison, S Brewer, et al. (2011) Pollen-based continental climate
708 reconstructions at 6 and 21 ka: a global synthesis. Clim Dyn 37: 775–802
709 Bartlein PJ, SL Shafer (2019) Paleo calendar-effect adjustments in time-slice and transient
710 climate-model simulations (PaleoCalAdjust v1.0): impact and strategies for data
711 analysis. Geosci Model Dev 12:3889–3913
712 Behera SK, JJ Luo, S Masson, SA Rao, H Sakuma, T Yamagata (2006) A CGCM study on
713 the interaction between IOD and ENSO. J Clim 19:1608–1705
714 Boschat G, P Terray, S Masson (2011) Interannual relationships between Indian summer
715 monsoon and Indo-Pacific coupled modes of variability during recent decades. Clim
716 Dyn 37:1019–1043

717 Boschat G, P Terray, S Masson (2012) Robustness of SST teleconnections and precursory
718 patterns associated with the Indian summer monsoon. Clim Dyn 38:2143–2165
719 Braconnot P, B Otto-Bliesner, SP Harrison, et al. (2007a) Results of PMIP2 coupled
720 simulations of the Mid-Holocene and Last Glacial Maximum – Part 1: experiments and
721 large-scale features. Clim Past 3:261–277
722 Braconnot P, B Otto-Bliesner, SP Harrison, et al. (2007b) Results of PMIP2 coupled
723 simulations of the Mid-Holocene and Last Glacial Maximum – Part 2: feedbacks with
724 emphasis on the location of the ITCZ and mid- and high latitudes heat budget. Clim
725 Past 3:279–296
726 Braconnot P, Y Luan, S Brewer, W Zheng (2012) Impact of Earth's orbit and freshwater
727 fluxes on Holocene climate mean seasonal cycle and ENSO characteristics. Clim Dyn
728 38:1081–1092
729 Braconnot P, D Zhu, O Marti, J Servonnat (2019a) Strengths and challenges for transient
730 Mid- to Late Holocene simulations with dynamical vegetation. Clim Past 15:997–1024
731 Braconnot P, J Crétat, O Marti, et al. (2019b) Impact of Multiscale Variability on Last 6,000
732 Years Indian and West African Monsoon Rain. GRL, doi:10.1029/2019GL084797
733 Carré M, JP Sachs, S Purca, et al. (2014) Holocene history of ENSO variance and asymmetry
734 in the eastern tropical Pacific. Science Rep, doi:10.1126/science.1252220
735 Chen L, L Wang, T Li, J Liu (2019) Drivers of reduced ENSO variability in mid-Holocene in
736 a coupled mode. Clim Dyn 52:5999–6014
737 Cobb KM, N Westphal, HR Sayani, et al. (2013) Highly variable El Niño-Southern
738 Oscillation throughout the Holocene. Science 339:67–70
739 Crétat J, P Terray, S Masson, PV Sooraj, MK Roxy (2017) Indian Ocean and Indian Summer
740 Monsoon : relationships without ENSO in ocean-atmosphere coupled simulations. Clim
741 Dyn 49:1429–1448

742 Crétat J, P Terray, S Masson, KP Sooraj (2018) Intrinsic precursors and timescale of the
743 tropical Indian Ocean Dipole: insights from partially decoupled numerical experiment.
744 Clim Dyn 51:1311–1332
745 Crétat J, B Pohl, B Dieppois, S Berthou, J Pergaud (2019) The Angola Low: relationship with
746 southern African rainfall and ENSO. Clim Dyn 52:1783–1803
747 Dallmeyer A, M Claussen, N Fischer, et al. (2015) The evolution of sub-monsoon systems in
748 the Afro-Asian monsoon region during the Holocene. Clim Past 11:305–326
749 Dallmeyer A, M Claussen, SJ Lorenz, T Shanahan (2019) The end of the African humid
750 period as seen by a transient comprehensive Earth system model simulation of the last
751 8000 years. Clim Past, doi:10.5194/cp-2019-86
752 Dufresne JL, MA Foujols, S Denvil, et al. (2013) Climate change projections using the IPSL-
753 CM5 Earth System Model: from CMIP3 to CMIP5. Clim Dyn 40:2123–2165
754 Emile-Geay J, KM Cobb, M Carré, et al. (2015) Links between tropical Pacific seasonal,
755 interannual and orbital variability during the Holocene. Nature Geo,
756 doi:10.1038/NGEO2608
757 Enfield DB, AM Mestas-Nuñez, PJ Trimble (2001) The Atlantic Multidecadal Oscillation and
758 its relation to rainfall and river flows in the continental US. Geophys Res Lett 28:2077–
759 2080
760 Fischer N, JH Jungclaus (2011) Evolution of the seasonal temperature cycle in a transient
761 Holocene simulation: orbital forcing and sea-ice. Clim Past 7:1139–1148
762 Gadgil S, PN Vinayachandran, PA Francis, S Gadgil (2004) Extremes of the Indian summer
763 monsoon rainfall, ENSO and equatorial Indian Ocean oscillation. Geophys Res Lett 31,
764 L12213, doi:10.1029/2004GL019733
765 Giesche A, M Staubwasser, CA Petrie, DA Hodell (2019) Indian winter and summer
766 monsoon strength over the 4.2 ka BP event in foraminifer isotope records from the

767 Indus River delta in the Arabian Sea. Clim Past 15:73–90
768 Gong X, MB Richman (1995) On the application of cluster analysis to growing season
769 precipitation data in North America East of the Rockies. J Clim 8:897–931
770 Goswami BB, BN Goswami (2017) A road map for improving dry‐bias in simulating the
771 South Asian monsoon precipitation by climate models. Clim Dyn 49:2025–2034
772 Harris I, PD Jones, TJ Osborn, DH Lister (2014) Updated high-resolution grids of monthly
773 climatic observations – the CRU TS3.10 Dataset. Int J Climatol 34:623–642
774 Harrison SP, PJ Bartlein, K Izumi, et al. (2015) Evaluation of CMIP5 palaeo-simulations to
775 improve climate projections. Nature Clim Change 5:735–743
776 Jalihal C, J Srinivasan, A Chakraborty (2019) Modulation of Indian monsoon by water vapor
777 and cloud feedback over the past 22,000 years. Nature Commun 10, 5701,
778 doi:10.1038/s41467-019-13754-6
779 Joshi MK, F Kucharski (2017) Impact of Interdecadal Pacific Oscillation on Indian summer
780 monsoon rainfall: An assessment from CMIP5 climate models. Clim Dyn 48:2375–
781 2391
782 Joussaume S, P Braconnot (1997) Sensitivity of paleoclimate simulation results to season
783 definitions. J Geophys Res 102:1943-1956
784 Joussaume S, KE Taylor, P Braconnot, et al. (1999) Monsoon changes for 5000 years ago:
785 Results of 18 simulations from the Paleoclimate Modeling Intercomparison Project
786 (PMIP). Geophys Res Lett 26:859–862
787 Kageyama M, P Braconnot, L Bopp, et al. (2013a) Mid-Holocene and Last Glacial Maximum
788 climate simulations with the IPSL model—part I: comparing IPSL_CM5A to
789 IPSL_CM4. Clim Dyn 40:2447–2468
790 Kageyama M, P Braconnot, L Bopp, et al. (2013b) Mid-Holocene and last glacial maximum
791 climate simulations with the IPSL model: part II: model-data comparisons. Clim Dyn

792 40:2469–2495
793 Kathayat G, H Cheng, A Sinha, et al. (2016) Indian monsoon variability on millennial-orbital
794 timescales. Sci Rep 6, 24374, doi:10.1038/srep24374
795 Kathayat G, H Cheng, A Sinha, et al. (2017) The Indian monsoon variability and civilization
796 changes in the Indian subcontinent. Science Adv 3: e1701296
797 Kaushal N, SFM Breitenbach, FA Lechleitner, et al. (2018) The Indian Summer Monsoon
798 from a Speleothem δ18O Perspective—A Review. Quat 29, doi:10.3390/quat1030029
799 Krishnamurthy L, Krishnamurthy V (2013) Influence of PDO on South Asian summer
800 monsoon-ENSO relation. Clim Dyn 42:2397–2410
801 Krishnan R, M Sugi M (2003) Pacific decadal oscillation and variability of the Indian summer
802 monsoon rainfall. Clim Dyn 21:233–242
803 Kug JS, Ham YG (2012) Indian Ocean feedback to the ENSO transition in a multi-model
804 ensemble. J Clim 25:6942–6957
805
806 Kumar P, J Sanwal, AP Dimri, R Ramesh (2019) Contribution of diverse monsoon
807 precipitation over Central and Northern India during mid to Late Holocene. Quat Int
808 507:217–223
809 Kutzbach JE (1981) Monsoon climate of the early Holocene: climate experiment with the
810 Earth's orbital parameters for 9000 years ago. Science 214, 59–61; erratum 214, 606
811 Kwiatkowski C, M Prange, V Varma, S Steinke, D Hebbeln, M Mohtadi (2015) Holocene
812 variations of thermocline conditions in the eastern tropical Indian Ocean. Quat Sci Rev
813 114: 33–42
814 Lézine AM, SJ Ivory, P Braconnot, O Marti (2017) Timing of the southward retreat of the
815 ITCZ at the end of the Holocene Humid Period in Southern Arabia: Data-model
816 comparison. Quat Sci Rev 164:68–76
817 Li G, Y Jian, S Yang et al. (2019) Effect of excessive equatorial Pacific cold tongue bias on

818 the El Niño-Northwest Pacific summer monsoon relationship in CMIP5 multi-model
819 ensemble. Clim Dyn 52:6195–6212
820 Liu Z, Otto-Bliesner B, Kutzbach J, Li L, Shields C (2003) Coupled climate simulation of the
821 evolution of global monsoons in the Holocene. J Clim 16:2472–2490
822 Liu Z, BL Otto-Bliesner, F He, et al. (2009) Transient Simulation of Last Deglaciation with a
823 New Mechanism for Bølling-Allerød Warming. Science 325:310–314
824 Lorenz SJ, G Lohmann (2004) Acceleration technique for Milankovitch type forcing in a
825 coupled atmosphere-ocean circulation model: method and application for the Holocene.
826 Clim Dyn 23:727–743
827 Lorenz SJ, JH Kim, N Rimbu, RR Schneider, G Lohmann (2006) Orbitally driven insolation
828 forcing on Holocene climate trends: Evidence from alkenone data and climate
829 modeling. Paleooceano 21, PA1002, doi:10.1029/2005PA001152
830 Madec G, R Bourdall_e-Badie, P Bouttier, C Bricaud, D Bruciaferri, D Calvert, M
831 Vancoppenolle (2017) NEMO ocean engine (version v3.6). Notes du Pôle de
832 modélisation de l'Institut Pierre-Simon Laplace (IPSL). doi: 10.5281/zenodo.1472492
833 Malik A, Brönnimann S, Stickler A, Raible CC, Muthers S, Anet J, Rozanov E, Schmutz W
834 (2017) Decadal to multidecadal scale variability of Indian summer monsoon rainfall in
835 the Coupled Ocean-Atmosphere-Chemistry Climate Model SOCOL-MPIOM. Clim Dyn
836 49:3551–3572
837 Malik A, S Brönnimann (2018) Factors affecting the inter-annual to centennial timescale
838 variability of Indian summer monsoon rainfall. Clim Dyn 50:4347–4364
839 Mantua NJ, SR Hare, Y Zhang, JM Wallace, RC Francis (1997) A Pacific interdecadal
840 climate oscillation with impacts on salmon production. Bull Amer Meteor Soc 78:1069-
841 1079
842 Marti O, P Braconnot, JL Dufresne, et al. (2010) Key features of the IPSL ocean atmosphere

model and its sensitivity to atmospheric resolution. Clim Dyn 34:1–26

Marzin C, P Braconnot (2009) Variations of Indian and African monsoons induced by insolation changes at 6 and 9.5 kyr BP. Clim Dyn 33:215-231

Otto-Bliesner BL, P Braconnot, SP Harrison, et al. (2016) The PMIP4 contribution to CMIP6 - Part 2: Two Interglacials, Scientific Objective and Experimental Design for Holocene and Last Interglacial Simulations. Geosci Model Dev Discuss 1-36, doi:10.5194/gmd-2016-279

Parthasarathy B, AA Munot, DR Kothawale (1995) All India monthly and seasonal rainfall series: 1871–1993. Theor Appl Climatol 49:217–224

Philander SGH (1983) El Niño Southern Oscillation phenomena. Nature, 302:295–301

Prodhomme C, P Terray, S Masson, G Boschat, T Izumo (2015) Oceanic factors controlling the Indian Summer Monsoon Onset in a coupled model. Clim Dyn 44: 977–1002

Kesava Rao AVR, SP Wani, K Srinivas (2020) Climate Change Impacts at Benchmark Watershed. In: Wani S., Raju K. (eds) Community and Climate Resilience in the Semi-Arid Tropics. Springer, Cham

Rasmusson EM, TH Carpenter (1983) The relationship between eastern equatorial Pacific sea surface temperatures and rainfall over India and Sri Lanka. J Clim 111:517–528

Rayner NA, DE Parker, EB Horton, et al. (2003) Global analyses of sea surface temperature, sea ice, and night marine air temperature since the late nineteenth century. J Geophys Res 108, doi:10.1029/2002JD002670

Roxy MK, ST Chaithra (2018) Impacts of Climate Change on the Indian Summer Monsoon. In book: Climate Change and Water Resources in India. Publisher: Ministry of Environment, Forest and Climate Change (MoEF&CC), Government of India

Roy SS, GB Goodrich, RC Balling Jr (2003) Influence of El Nino/Southern oscillation, Pacific Decadal Oscillation, and local sea-surface temperature anomalies on peak

season monsoon precipitation in India. Clim Res 25:171–178

Saji NH, BN Goswami, PN Vinayachandran, T Yamagata (1999) A dipole mode in the tropical Indian Ocean. Nature, 401:360–363

Sepulchre P, A Caubel, JB Ladant, et al. (2019) IPSL-CM5A2. An Earth System Model designed for multi-millennial climate simulations. Geosci Model Dev Discuss, doi:10.5194/gmd-2019-332

Shi J, Q Yan (2019) Evolution of the Asian–African Monsoonal Precipitation over the last 21 kyr and the Associated Dynamic Mechanisms. J Clim, doi:10.1175/JCLI-D-19-0074.1

Sikka DR (1980) Some aspects of the large-scale fluctuations of summer monsoon rainfall over India in relation to fluctuations in the planetary and regional scale circulation parameters. Proc Indian Acad Sci Earth Planet Sci 89:179–195

Sooraj KP, P Terray, S Masson, J Crétat (2019) Modulations of the Indian summer monsoon by the hot subtropical deserts: insights from sensitivity experiments. Clim Dyn 52:4527–4555

Sperber KR, H Annamalai, IS Kang, A Kitoh, A Moise, A Turner, B Wang, T Zhou (2013) The Asian summer monsoon: an intercomparison of CMIP5 vs. CMIP3 simulations of the late 20th century. Clim Dyn 41:2711–2744

Staubwasser M, F Sirocko, PM Grootes, M Segl (2003) Climate change at the 4.2 ka BP termination of the Indus valley civilization and Holocene south Asian monsoon variability. Geophys Res Lett 30, doi:10.1029/2002GL016822

Terray P, E Guilyardi, AS Fischer, P Delecluse (2005) Dynamics of Indian Monsoon and ENSO Relationships in the SINTEX global Coupled Model. Clim Dyn 24: 145–168

Terray P, KP Sooraj, S Masson, RPM Krishna, G Samson and AG Prajeesh (2018) Towards a realistic simulation of boreal summer tropical raihfall climatology in state-of-the art coupled models: role of the background snow-free albedo. Clim Dyn 50:3413–3439

893 Terray P, KP Sooraj, S Masson, C Prodhomme (2020) Anatomy of the Indian Summer
894 Monsoon and ENSO relationships in state-of-the-art CGCMs: Role of the tropical
895 Indian Ocean. Submitted to Clim Dyn
896 Varma V, M Prange, U Merkel, T Kleinen, G Lohmann, M Pfeiffer, H Renssen, A Wagner, S
897 Wagner, M Schulz (2012) Holocene evolution of the Southern Hemisphere westerly
898 winds in transient simulations with global climate models. Clim Past 8:391–402
899 Varma V, M Prange, M Schulz (2016) Transient simulations of the present and the last
900 interglacial climate using the Community Climate System Model version 3: effects of
901 orbital acceleration. Geosci Model Dev 9:3859–3873
902 Walker GT (1924) Correlations in seasonal variations of weather. I. A further study of world
903 weather. Mem Indian Meteorol Dep 24:275–332
904 Wang B, QH Ding, XH Fu, IS Kang, K Jin, J Shukla, F Doblas-Reyes (2005) Fundamental
905 challenge in simulation and prediction of summer monsoon rainfall. Geophys Res Lett
906 32, L15711, doi:10.1029/2005GL022734
907 Ward JH (1963) Hierarchical grouping to optimize an objective function. J Am Stat Assoc
908 58:236–244
909 White SM, AC Ravelo, PJ Polissa (2018) Dampened El Niño in the Early and Mid-Holocene
910 Due To Insolation-Forced Warming/Deepening of the Thermocline. Geophys Res Let
911 45, doi:10.1002/ 2017GL075433
912 Yan M, J Liu (2019) Physical processes of cooling and mega-drought during the 4.2 ka BP
913 event: results from TraCE-21ka simulations. Clim Past 15:265–277
914 Zhao Y, P Braconnot, O Marti, et al. (2005) A Multi-model analysis of the role of the ocean
915 on the African and Indian monsoon during the mid-Holocene. Clim Dyn 25:777–800
916 Zhao Y, SP Harrison (2012) Mid-Holocene monsoons: a multi-model analysis of the inter-
917 hemispheric differences in the responses to orbital forcing and ocean feedbacks. Clim

Dyn 39:1457–1487

Table Captions

Table 1: Major differences in model set up between the five simulations analyzed in this study. All simulations have the ORCA 2° ocean grid with 31 vertical levels. The LR and MR resolutions stand for the atmospheric horizontal resolution. The LR (MR) atmosphere resolution is 3.75° (2.5°) in longitude and 1.875° (1.25°) in latitude with 39 vertical levels in both LR and MR. See main text for the description of the model version, the land surface, the land-ocean river runoff and the experimental design for prescribing or computing vegetation.

Table 2: Mean-state and variability of July-to-September seasonal ISMR (land points in the 5°-25°N – 77°-88°E region) for the 1871-2012 AIR, 1979-2010 GPCP and 1901-2016 CRU data and for the last 100 years of the two simulations (1851-1950). Variability is computed as the standard-deviation of JJAS rainfall anomalies. Values in parenthesis correspond to the standard-deviation of the results obtained for the 123, 97 and 81 20-yr windows of the AIR, CRU and two simulations.

Table 3: Number of patterns (and percentage) within each of the six ISMR regimes after removing the outliers. The percentage in the first column is expressed against the total number of classified patterns. The percentage in the remaining columns corresponds to the weight each simulation has on the total number of patterns spent in each ISMR regime (given in the first column).

Figure Captions

Figure 1: (a) Mean seasonal cycle of monthly rainfall area-averaged over India (land points within the 5°-25°N – 70°-88°E region) for the 1871-2012 AIR and 1901-2016 CRU and 1979-2010 GPCP data, and the last 100 years of the TR5AS-Vlr01 and TR6AV-Sr02 simulations (i.e., 1851-1950). For the AIR data and the two simulations, thin curves show sampling errors defined as the mean seasonal cycle of all possible 20-yr windows along the 1871-2012 and 1851-1950 period, respectively. (b) Same as (a) but for Indian rainfall variability defined as the standard-deviation of rainfall anomalies.

Figure 2: Location of the 2 mm/day isohyet from April to September for the (a) 1979-2010 GPCP and (b) 1901-2016 CRU data and the last 100 years (i.e., 1851-1950) of the (c) TR5AS-Vlr01 and (d) TR6AV-Sr02 simulations.

Figure 3: Mid- to late Holocene changes in the (a-b) mean-state and (c-d) variability of rainfall area-averaged over India for the TR5AS-Vlr01 and TR6AV-Sr02 simulations. Both mean-state and variability are computed along 100-yr adjacent windows. (e-h) Relative differences in rainfall mean-state between the four TR6 simulations and their ensemble mean for each 100-yr adjacent from 6 to 3.8 kyr BP.

Figure 4: (a-b) PDF of JJAS rainfall area-averaged over India computed along each 100-yr adjacent window for the TR5AS-Vlr01 and TR6AV-Sr02 simulations, respectively. Blue-to-red colors show the evolution of the PDFs from mid- to late Holocene. (c) Evolution of the 10^{th} and 90^{th} percentile threshold values of ISMR anomalies for the five simulations. The percentile threshold values for each simulation are computed along each 100-yr moving window with 1-year increment between each window, giving one value for each year, and are displayed as ISMR departures from the first 100-yr climatology to remove offset differences between the simulations induced by different initial conditions. (d-e) Evolution in the number of the 10% driest and 10% wettest ISMR seasons in each simulation defined using the 10^{th} and 90^{th} percentile threshold values from the first 100-yr window.

Figure 5: Snapshots of mid- to late Holocene significant changes in JJAS rainfall mean-state (dashed/solid contours for |0.2|, |1.5| and |3| mm/day dry/wet differences) and standard-deviation (shadings) for the TR6AV-Sr02 simulation. For each 100-yr adjacent window,

changes in mean-state and standard-deviation are computed as the departure from the first 100 years of the simulation (e.g. 6-5.9 kyr BP period) and significance is tested at the 95% confidence level according to a Student t test and a Chi-square test, respectively. (a) Mean and standard-deviation changes (averages on 4 100-yr adjacent windows) from 5.9 to 5.5 kyr BP that reach the 95% confidence level in at least 2 100-yr windows. (b-f) Same as (a) but for changes averaged on 5 100-yr consecutive windows from 5 to 4.5, 4 to 3.5, 3 to 2.5, 2 to 1.5 and 1 to 0.5 kyr BP time interval, respectively, that reach the 95% confidence level in at least 3 100-yr windows in the time interval.

Figure 6: Same as Fig. 5 but for changes in SST mean-state (dashed/solid contours for |0.1|, |0.4| and |1|°C cold/warm differences) and standard-deviation (shadings).

Figure 7: (a) Ensemble mean anomalous rainfall pattern associated to ISMR regime #1. Only rainfall anomalies that are significant at the 95% confidence level according to a Student t test are shown. (c-f) Same as (a) but for the 5 remaining ISMR regimes.

Figure 8: Same as Fig. 8 but for SST anomalies (°C), except significant SST anomalies are contoured in black.

Figure 9: Same as Fig. 8 but for 850-hPa wind anomalies (vectors; m/s) and associated divergence (shadings; m/s; blue = anomalous convergence; red = anomalous divergence). Wind anomalies are shown in black when at least one component (i.e., zonal or meridian) depict significant changes tested as in Fig. 8.

Figure 10: (a) Ensemble mean rainfall and SST anomalies associated with the six ISMR regimes identified by applying the AHC clustering to the last 100 years (i.e., 1851-1950) of the TR5AS-Vlr01 and TR6AV-Sr02 ensemble. Significant anomalies at the 95% confidence level according to a Student t test are contoured in black. (b) Same as (a) but for the CRU-HadISST data for the 1901-2016 period.

Figure 11: Model dependency in the mean anomalous rainfall pattern associated to the six ISMR regimes for (a-e) the five simulations. For each ISMR regime, model dependency is defined as the departure of the mean anomalous rainfall pattern of each simulation from the ensemble mean anomalous rainfall pattern shown in Fig. 8. Only departure significant at the

95% confidence level according to a Student t test is shown.

Figure 12: (a-f) Century-to-century evolution in the frequency of occurrence of the six ISMR regimes from 6 to 3.8 kyr BP for the five simulations. The frequency of occurrence is displayed as the departure from its mean value.

Figure 13: Century-to-century evolution in boreal summer (JJAS) SST variability of the (a) Niño3.4, (b) western tropical IO (10°S-10°N; 50°-70°E), (c) eastern equatorial IO (10°S-Eq; 90°-110°E) and (d) IOD indices from 6 to 3.8 kyr BP for the five simulations. Variability is defined as standard-deviation of SST anomalies for each 100-yr adjacent window. The variability is displayed as the departure from the mean value of the standard-deviations computed for each 100-yr adjacent window.

Figure 14: (a; upper panel) Century-to-century evolution in the frequency of occurrence of the ISMR regime associated to La Niña-like – IOD- collocation from 6 to 0 kyr BP for the TR6AV-Sr02 simulation. This ISMR regime is extracted by applying the AHC clustering to anomalous Indian rainfall patterns from 6 to 0 kyr BP in the two 6000-yr simulation ensemble (TR5AS-Vlr01 and TR6AV-Sr02) with a 6-regime cutoff. The frequency of occurrence is expressed as the departure from its mean value. (a; bottom panels) Number of occurrences of this ISMR regime along each 2000-yr adjacent window and associated mean anomalous SST patterns. Only SST anomalies significant at the 95% confidence level according to a Student t test are shown. (b) Same as (a) but for the ISMR regime associated to El Niño-like – IOD+ collocation.

Figure 15: (a) 4.9-3.8 minus 6-4.9 kyr BP differences in precipitable water, SST, moisture transport and evaporation ensemble mean anomalies associated to regime #3. Significant anomalies at the 95% confidence level according to a Student two-tailed t test are contoured in black for precipitable water, SST and evaporation and shown with black vectors for moisture transport. (b) Same as (a) but for regime #4.

Figure A1: (a) Dendrogram tree obtained at the end of the AHC procedure applied to JJAS rainfall anomalies simulated over India by the 5-simulation ensemble from 6 to 3.8 kyr BP. (b) Evolution of the similarity metric for the 10 last mergings. See Appendix A for details.

Tables

Simulation	Model version	Resolution	Land-surface	Dynamical vegetation	Land-ocean river runoff	Integration length
TR5AS-Vlr01	TR5A	LR	CM5	No – present	CM6	6,000 years
TR6AV-Sr02	TR6A	MR	11 layers	Yes	Inter	6,000 years
TR6AS-Sr10	TR6A	MR	11 layers	No – present	Inter	4,000 years
TR6AS-Sr11	TR6A	MR	11 layers	No – present	CM6	2,250 years
TR6AS-Sr12	TR6A	MR	11 layers	No – Mid-Holocene	Inter	2,250 years

Table 1: Major differences in model set up between the five simulations analyzed in this study. All simulations have the ORCA 2° ocean grid with 31 vertical levels. The LR and MR resolutions stand for the atmospheric horizontal resolution. The LR (MR) atmosphere resolution is 3.75° (2.5°) in longitude and 1.875° (1.25°) in latitude with 39 vertical levels in both LR and MR. See main text for the description of the model version, the land surface, the land-ocean river runoff and the experimental design for prescribing or computing vegetation.

	Mean State ($mm.day^{-1}$)	Variability ($mm.day^{-1}$)
AIR	6.93 (+/- 0.15)	1.22 (+/- 0.13)
GPCP	7.36	1.13
CRU	6.73 (+/- 0.15)	1.33 (+/- 0.10)
Vlr01	4.84 (+/- 0.18)	1.05 (+/- 0.11)
Sr02	5.72 (+/- 0.15)	1.34 (+/- 0.13)

Table 2: Mean-state and variability of July-to-September seasonal ISMR (land points in the 5°-25°N – 77°-88°E region) for the 1871-2012 AIR, 1979-2010 GPCP and 1901-2016 CRU data and for the last 100 years of the two simulations (1851-1950). Variability is computed as the standard-deviation of JJAS rainfall anomalies. Values in parenthesis correspond to the standard-deviation of the results obtained for the 123, 97 and 81 20-yr windows of the AIR, CRU and two simulations.

	Total	TR5AS-Vlr01	TR6AS-Sr10	TR6AS-Sr11	TR6AS-Sr12	TR6AV-Sr02
CL#1	1227 (13.7%)	333 (27.1)	199 (16.2)	221 (18)	238 (19.4)	236 (19.2)
CL#2	1344 (15%)	425 (31.6)	229 (17)	229 (17)	237 (17.6)	224 (16.7)
CL#3	1278 (14.2%)	131 (10.3)	280 (21.9)	292 (22.8)	296 (23.2)	279 (21.8)
CL#4	1821 (20.3%)	477 (26.2)	345 (18.9)	344 (18.9)	328 (18)	327 (18)
CL#5	933 (10.4%)	39 (4.2)	252 (27)	222 (23.8)	209 (22.4)	211 (22.6)
CL#6	2360 (26.3%)	288 (12.2)	489 (20.7)	518 (21.9)	521 (22.1)	544 (23.1)
Total	8963	1693	1794	1826	1829	1821

Table 3: Number of patterns (and percentage) within each of the 6 recurrent ISMR regimes after removing the outliers. The percentage in the first column is expressed against the total number of classified patterns. The percentage in the remaining columns corresponds to the weight each simulation has on the total number of patterns spent in each ISMR regime (given in the first column).

Figures

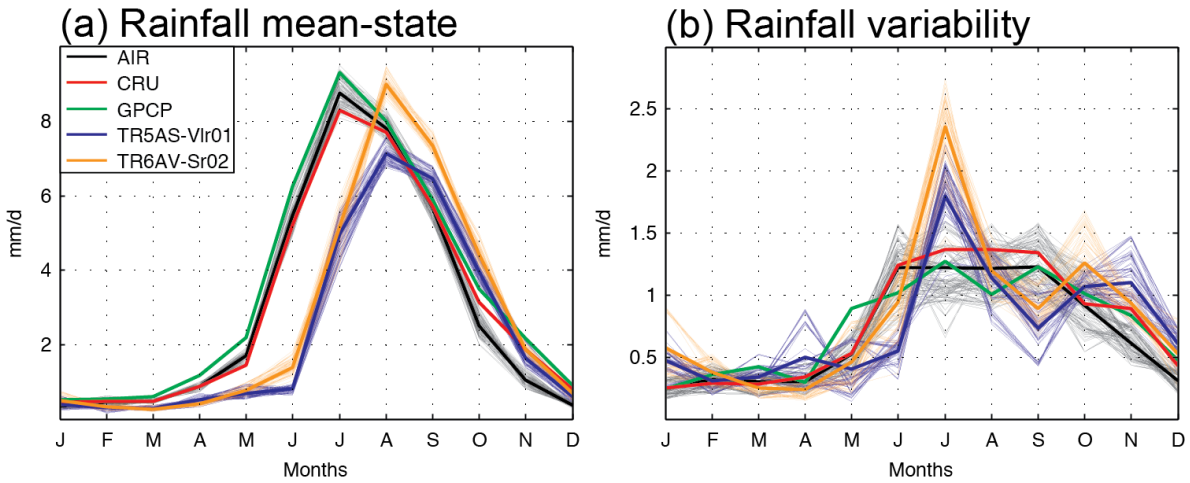

Figure 1: (a) Mean seasonal cycle of monthly rainfall area-averaged over India (land points within the 5°-25°N – 70°-88°E region) for the 1871-2012 AIR and 1901-2016 CRU and 1979-2010 GPCP data, and the last 100 years of the TR5AS-Vlr01 and TR6AV-Sr02 simulations (i.e., 1851-1950). For the AIR data and the two simulations, thin curves show sampling errors defined as the mean seasonal cycle of all possible 20-yr windows along the 1871-2012 and 1851-1950 period, respectively. (b) Same as (a) but for Indian rainfall variability defined as the standard-deviation of rainfall anomalies.

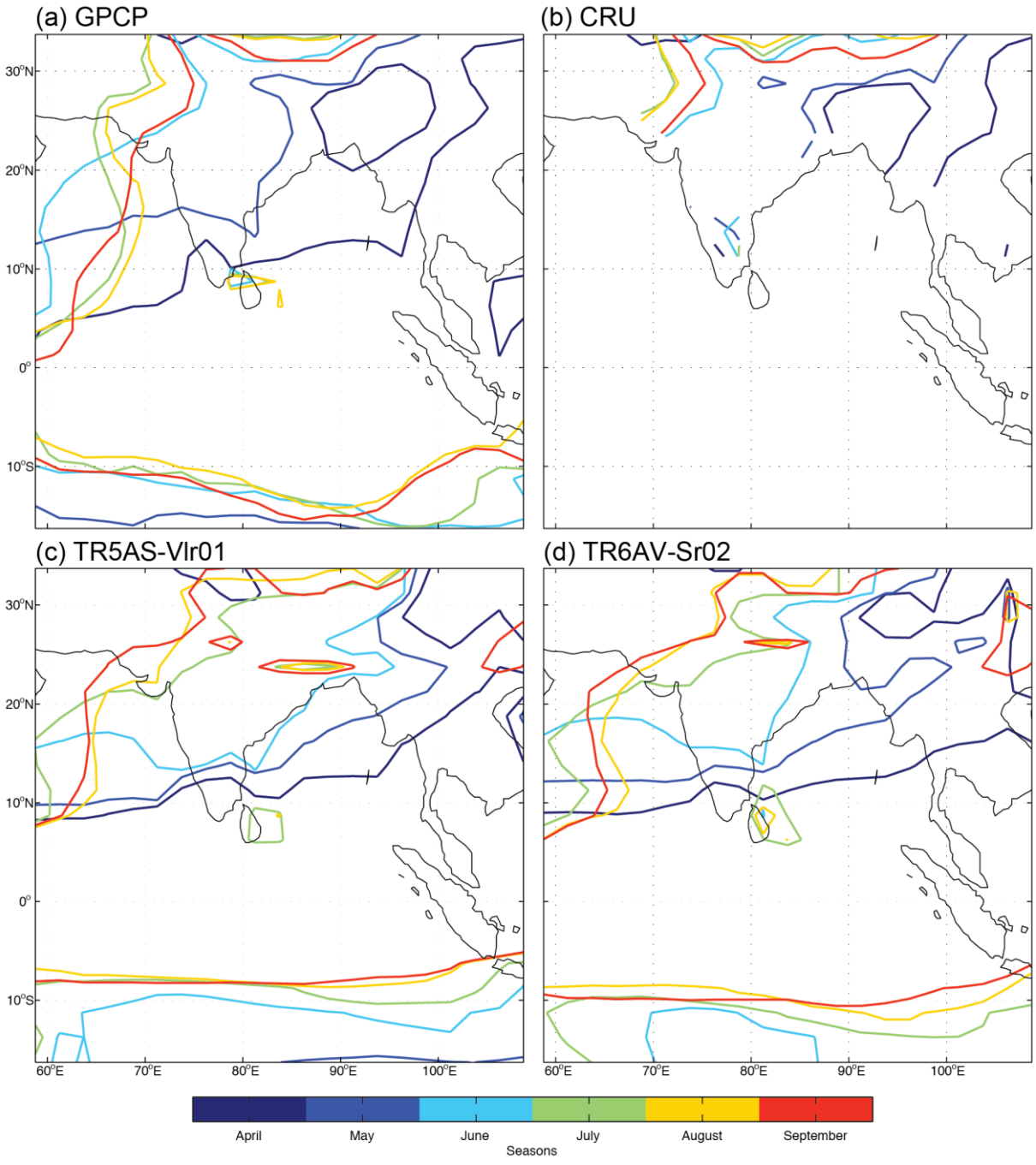

Figure 2: Location of the 2 mm/day isohyet from April to September for the (a) 1979-2010 GPCP and (b) 1901-2016 CRU data and the last 100 years (i.e., 1851-1950) of the (c) TR5AS-Vlr01 and (d) TR6AV-Sr02 simulations.

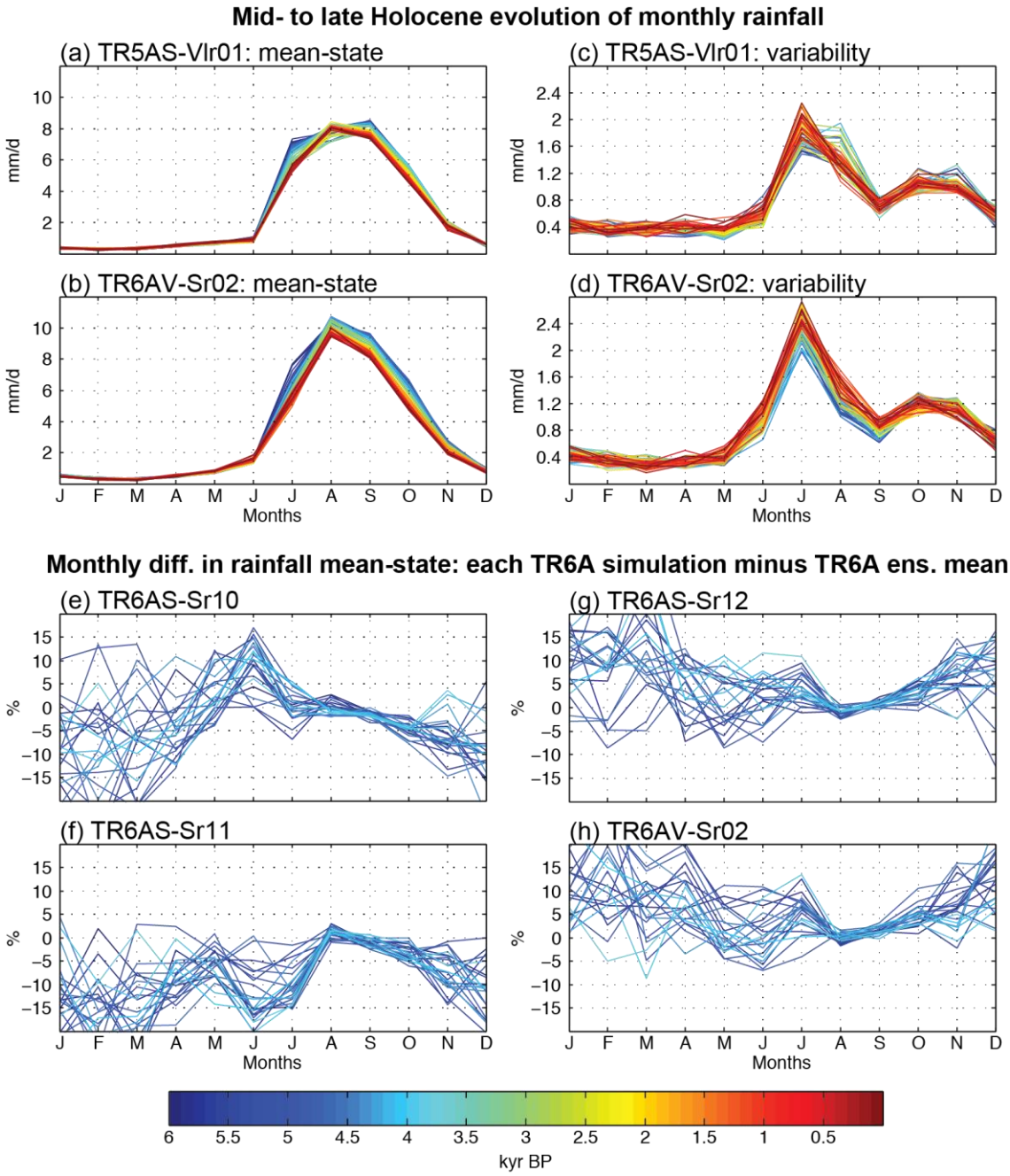

Figure 3: Mid- to late Holocene changes in the (a-b) mean-state and (c-d) variability of rainfall area-averaged over India for the TR5AS-Vlr01 and TR6AV-Sr02 simulations. Both mean-state and variability are computed along 100-yr adjacent windows. (e-h) Relative differences in rainfall mean-state between the four TR6 simulations and their ensemble mean for each 100-yr adjacent from 6 to 3.8 kyr BP.

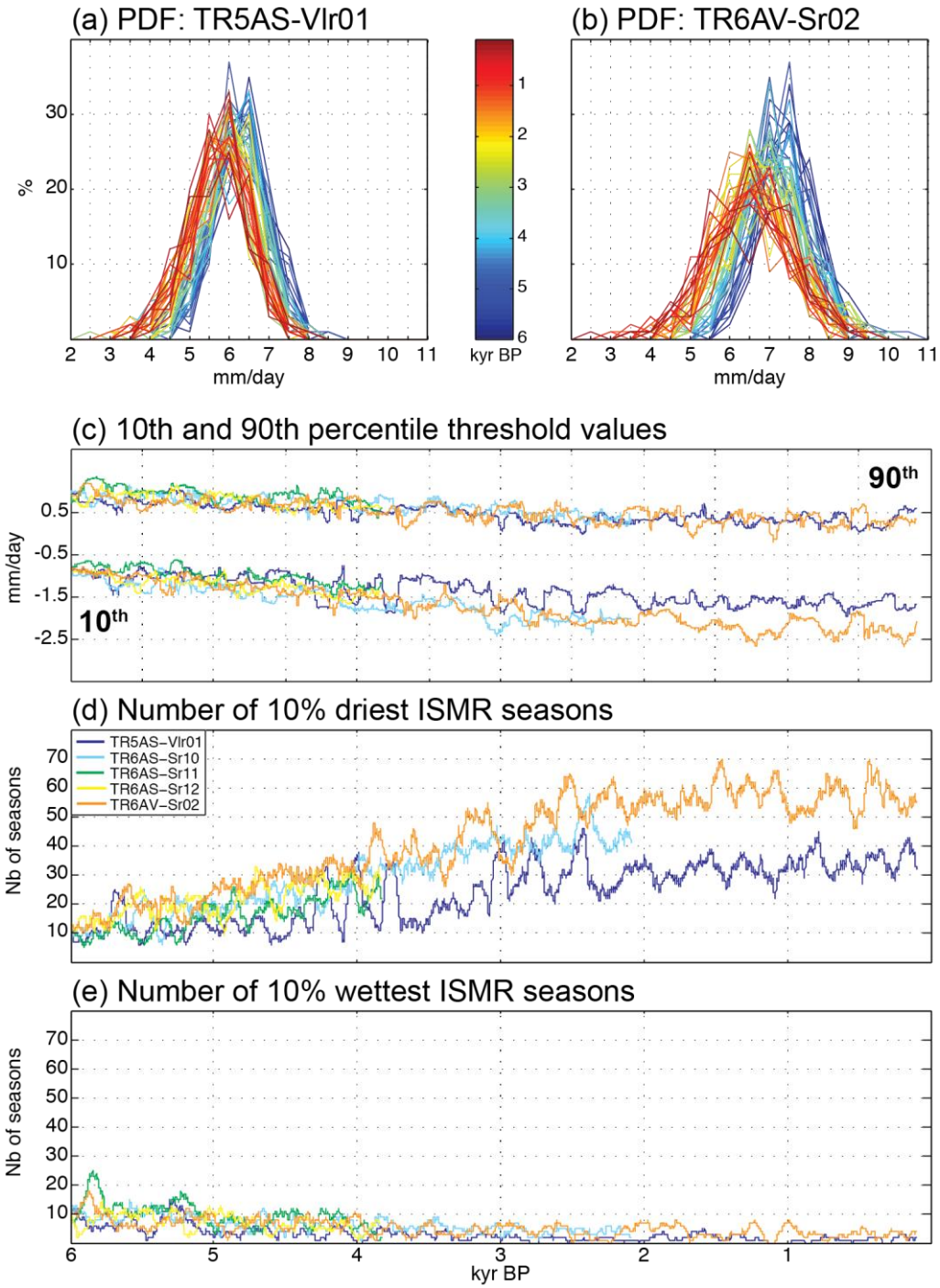

Figure 4: (a-b) PDF of JJAS rainfall area-averaged over India computed along each 100-yr adjacent window for the TR5AS-Vlr01 and TR6AV-Sr02 simulations, respectively. Blue-to-red colors show the evolution of the PDFs from mid- to late Holocene. (c) Evolution of the 10^{th} and 90^{th} percentile threshold values of ISMR anomalies for the five simulations. The percentile threshold values for each simulation are computed along each 100-yr moving window with 1-year increment between each window, giving one value for each year, and are displayed as ISMR departures from the first 100-yr climatology to remove offset differences between the simulations induced by different initial conditions. (d-e) Evolution in the number of the 10% driest and 10% wettest ISMR seasons in each simulation defined using the 10^{th} and 90^{th} percentile threshold values from the first 100-yr window.

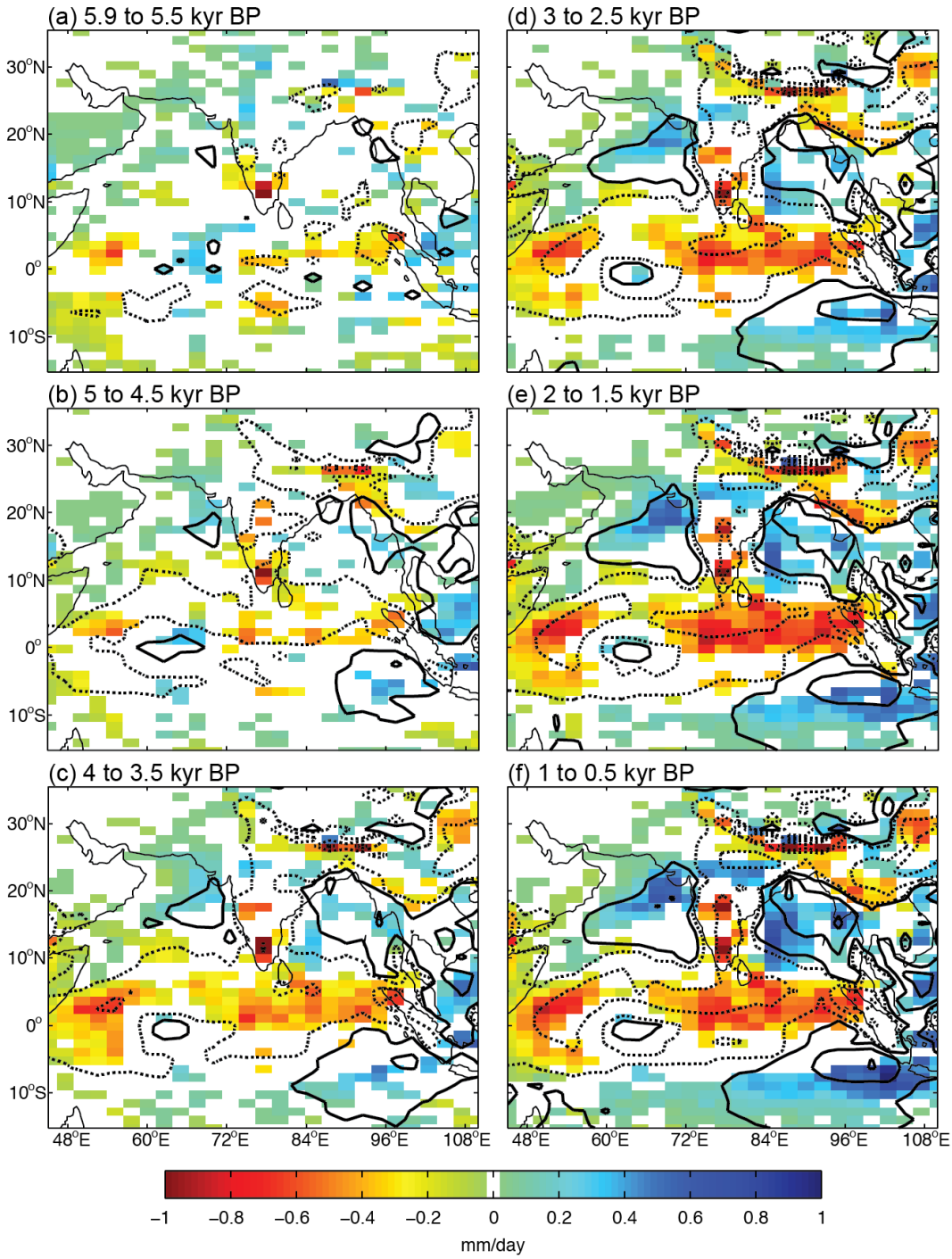

Figure 5: Snapshots of mid- to late Holocene significant changes in JJAS rainfall mean-state (dashed/solid contours for |0.2|, |1.5| and |3| mm/day dry/wet differences) and standard-deviation (shadings) for the TR6AV-Sr02 simulation. For each 100-yr adjacent window, changes in mean-state and standard-deviation are computed as the departure from the first 100 years of the simulation (e.g. 6-5.9 kyr BP period) and significance is tested at the 95% confidence level according to a Student t test and a Chi-square test, respectively. (a) Mean and standard-deviation changes (averages on 4 100-yr adjacent windows) from 5.9 to 5.5 kyr BP that reach the 95% confidence level in at least 2 100-yr windows. (b-f) Same as (a) but for changes averaged on 5 100-yr consecutive windows from 5 to 4.5, 4 to 3.5, 3 to 2.5, 2 to 1.5 and 1 to 0.5 kyr BP time interval, respectively, that reach the 95% confidence level in at least 3 100-yr windows in the time interval.

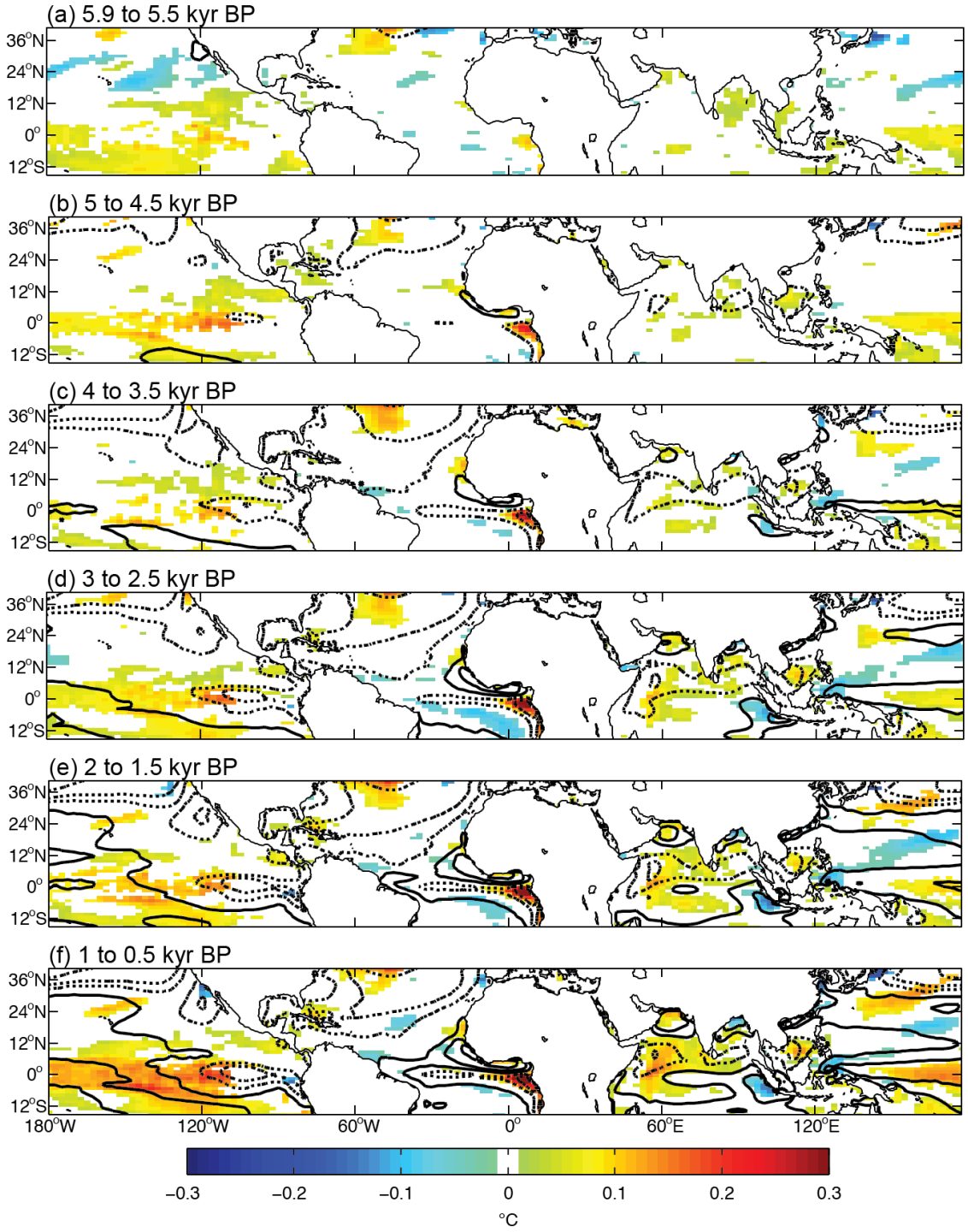

Figure 6: Same as Fig. 5 but for changes in SST mean-state (dashed/solid contours for |0.1|, |0.4| and |1|°C cold/warm differences) and standard-deviation (shadings).

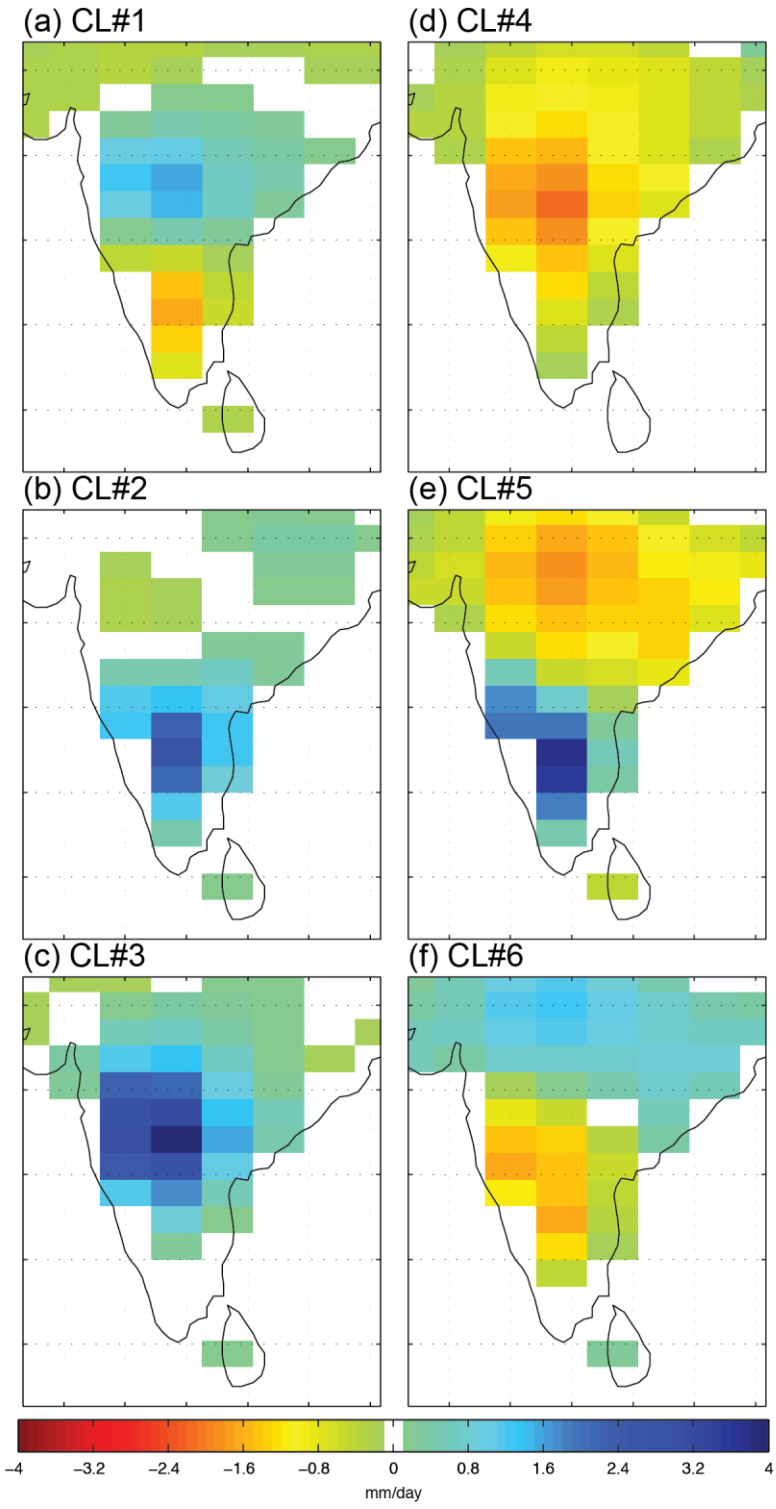

Figure 7: (a) Ensemble mean anomalous rainfall pattern associated to ISMR regime #1. Only rainfall anomalies that are significant at the 95% confidence level according to a Student t test are shown. (c-f) Same as (a) but for the 5 remaining ISMR regimes.

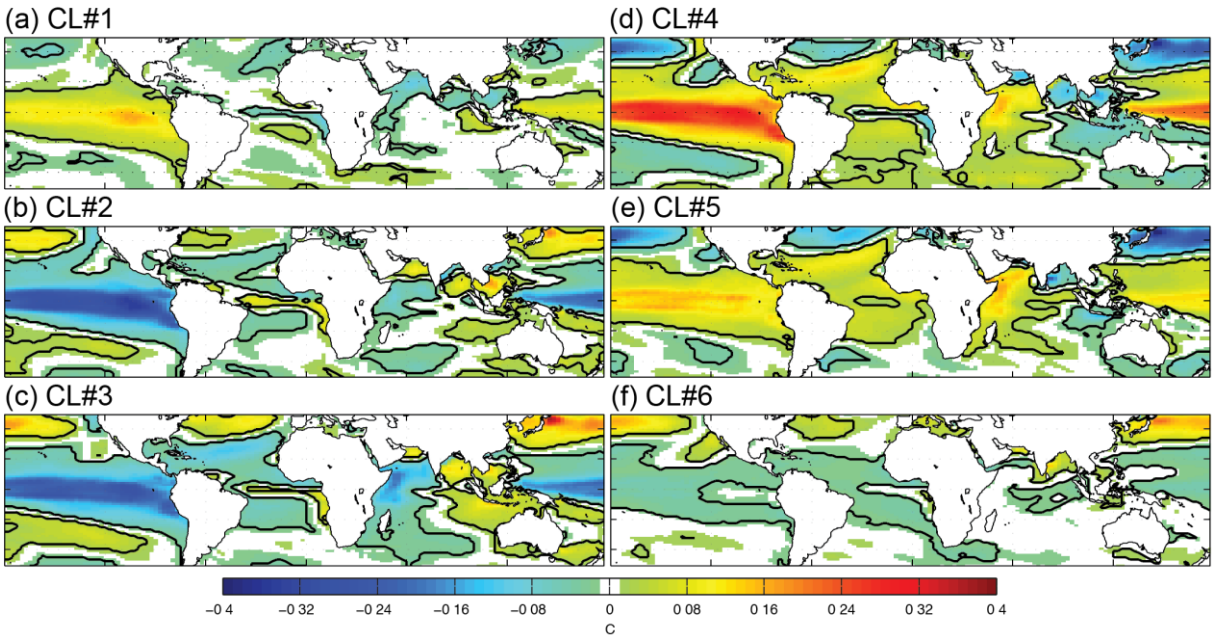

Figure 8: Same as Fig. 7 but for SST anomalies (°C), except significant SST anomalies are contoured in black.

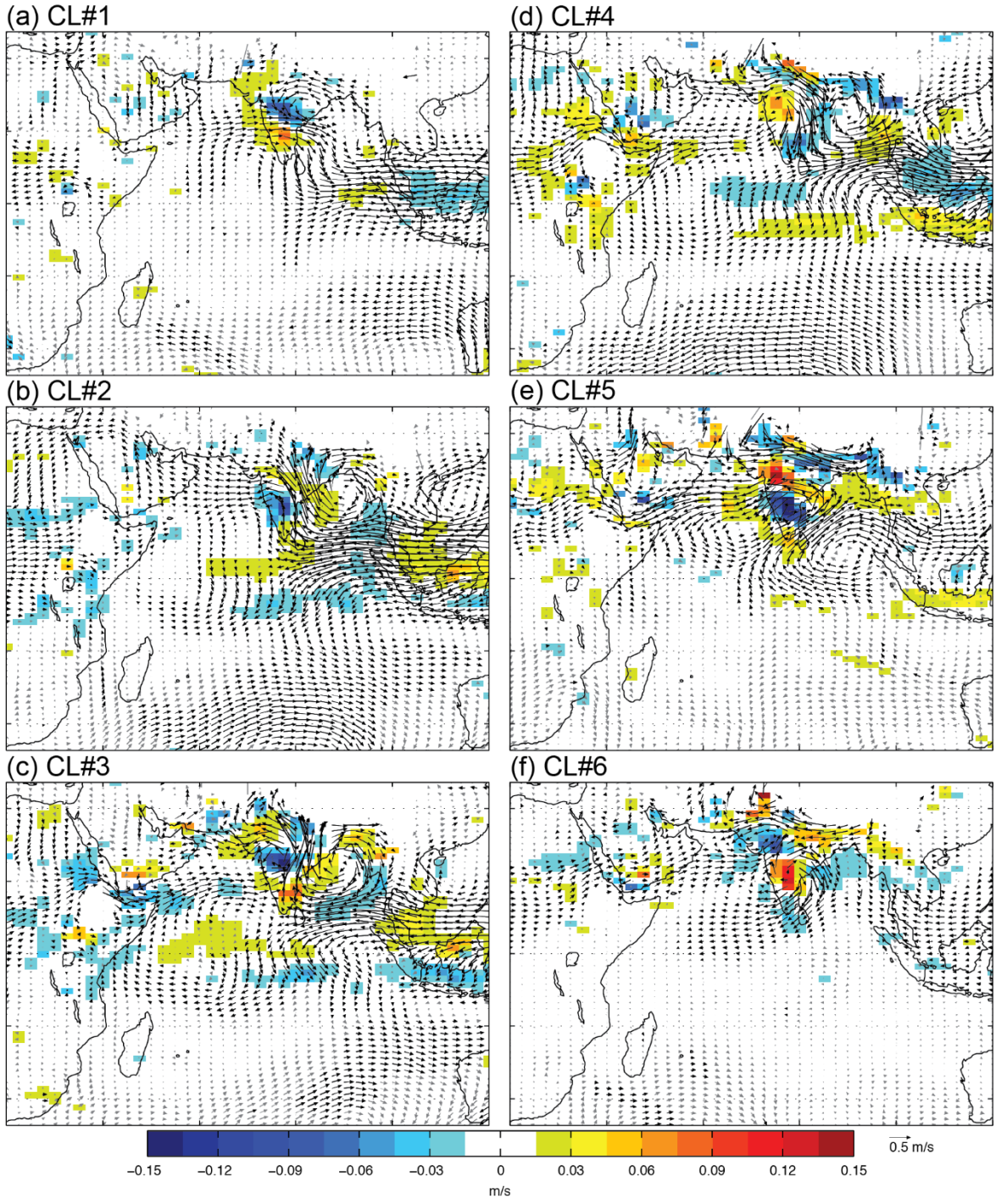

Figure 9: Same as Fig. 7 but for 850-hPa wind anomalies (vectors; m/s) and associated divergence (shadings; m/s; blue = anomalous convergence; red = anomalous divergence). Wind anomalies are shown in black when at least one component (i.e., zonal or meridian) depict significant changes tested as in Fig. 7.

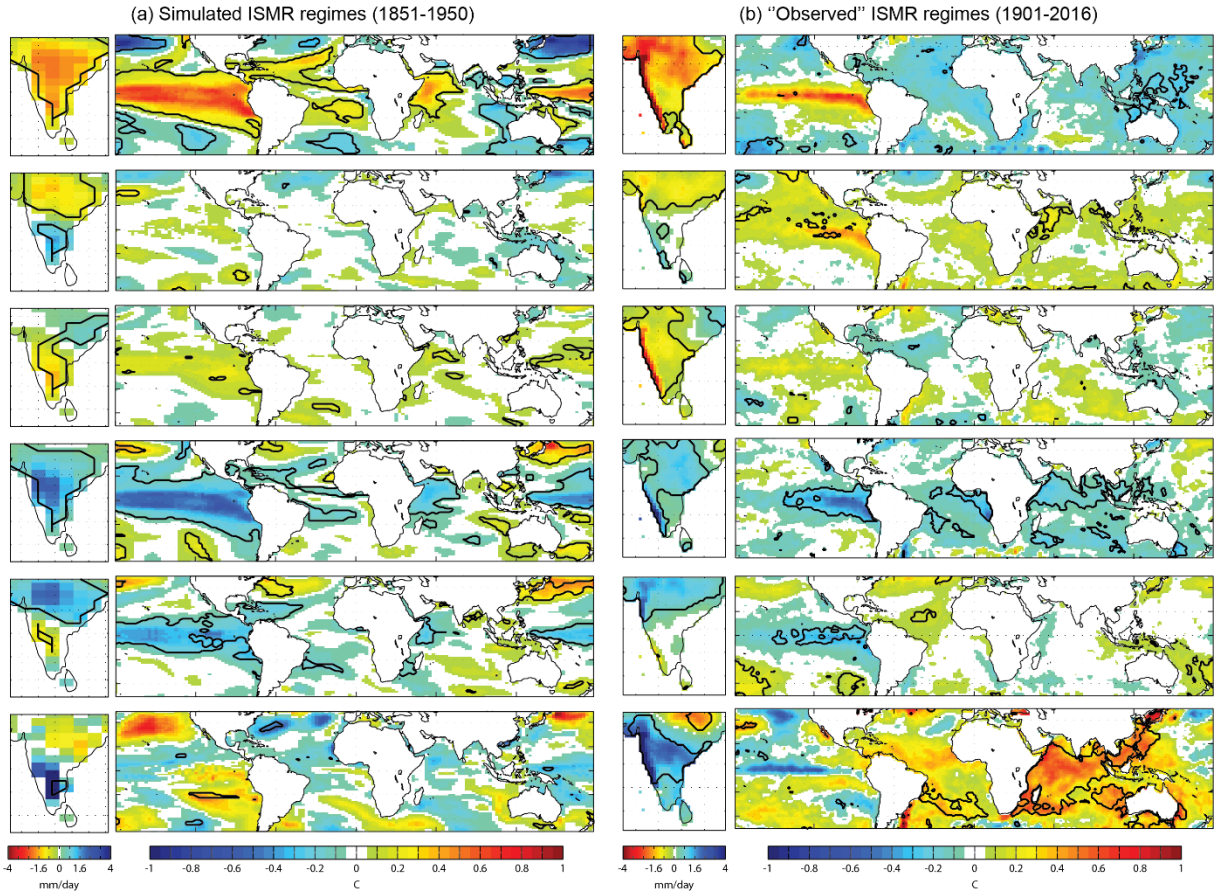

Figure 10: (a) Ensemble mean rainfall and SST anomalies associated with the six ISMR regimes identified by applying the AHC clustering to the last 100 years (i.e., 1851-1950) of the TR5AS-Vlr01 and TR6AV-Sr02 ensemble. Significant anomalies at the 95% confidence level according to a Student t test are contoured in black. (b) Same as (a) but for the CRU-HadISST data for the 1901-2016 period.

Figure 11: Model dependency in the mean anomalous rainfall pattern associated to the six ISMR regimes for (a-e) the five simulations. For each ISMR regime, model dependency is defined as the departure of the mean anomalous rainfall pattern of each simulation from the ensemble mean anomalous rainfall pattern shown in Fig. 7. Only departure significant at the 95% confidence level according to a Student t test is shown.

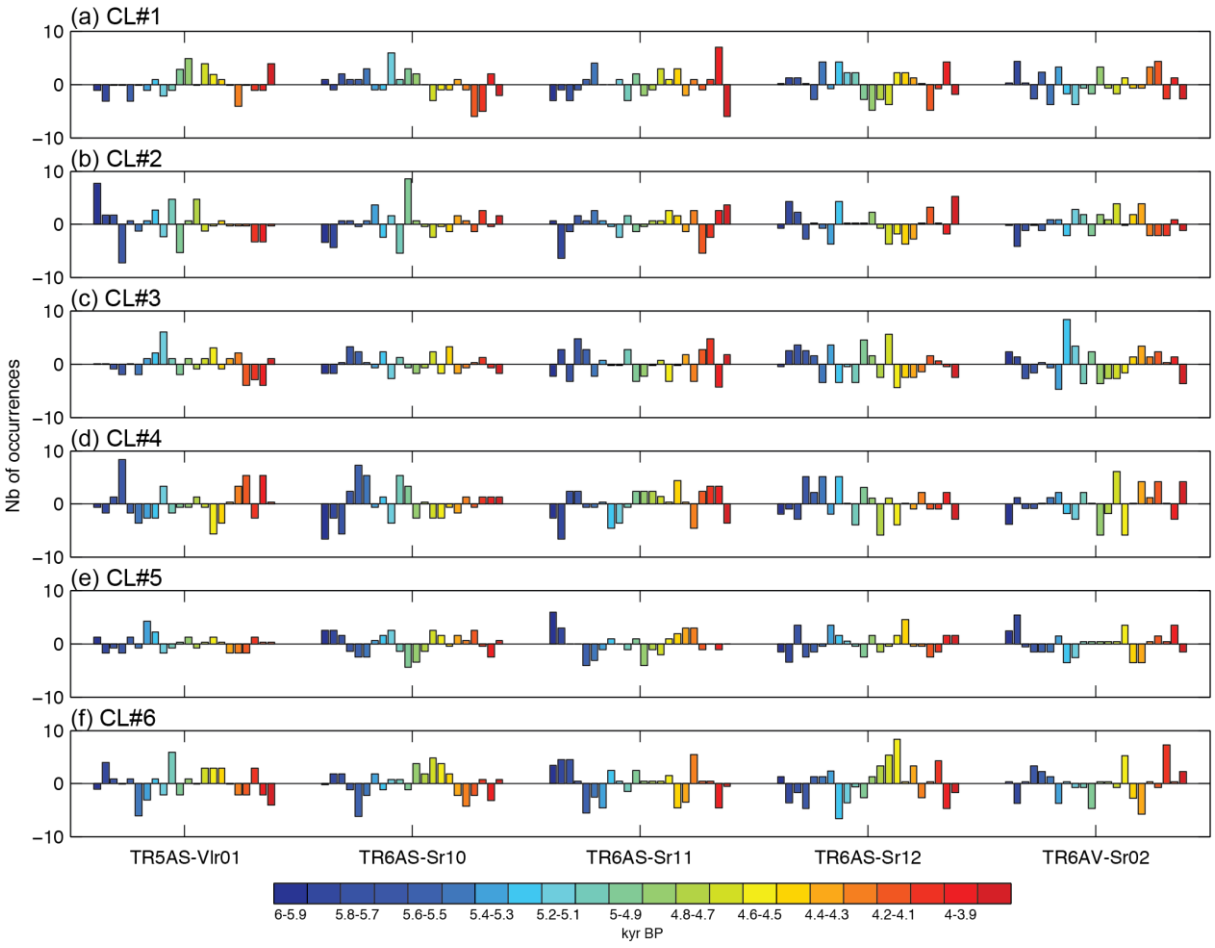

Figure 12: (a-f) Century-to-century evolution in the frequency of occurrence of the six ISMR regimes from 6 to 3.8 kyr BP for the five simulations. The frequency of occurrence is expressed as the departure from its mean value.

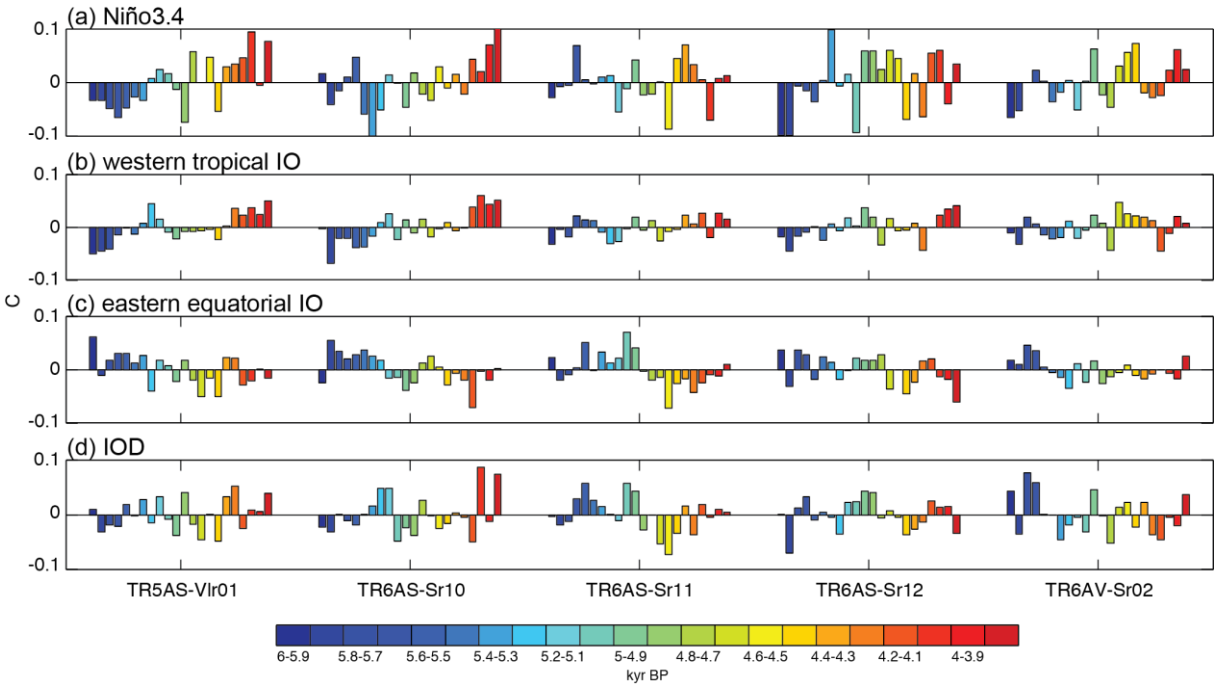

Figure 13: Century-to-century evolution in boreal summer (JJAS) SST variability of the (a) Niño3.4, (b) western tropical IO (10°S-10°N; 50°-70°E), (c) eastern equatorial IO (10°S-Eq; 90°-110°E) and (d) IOD indices from 6 to 3.8 kyr BP for the five simulations. Variability is defined as standard-deviation of SST anomalies for each 100-yr adjacent window. The variability is displayed as the departure from the mean value of the standard-deviations computed for each 100-yr adjacent window.

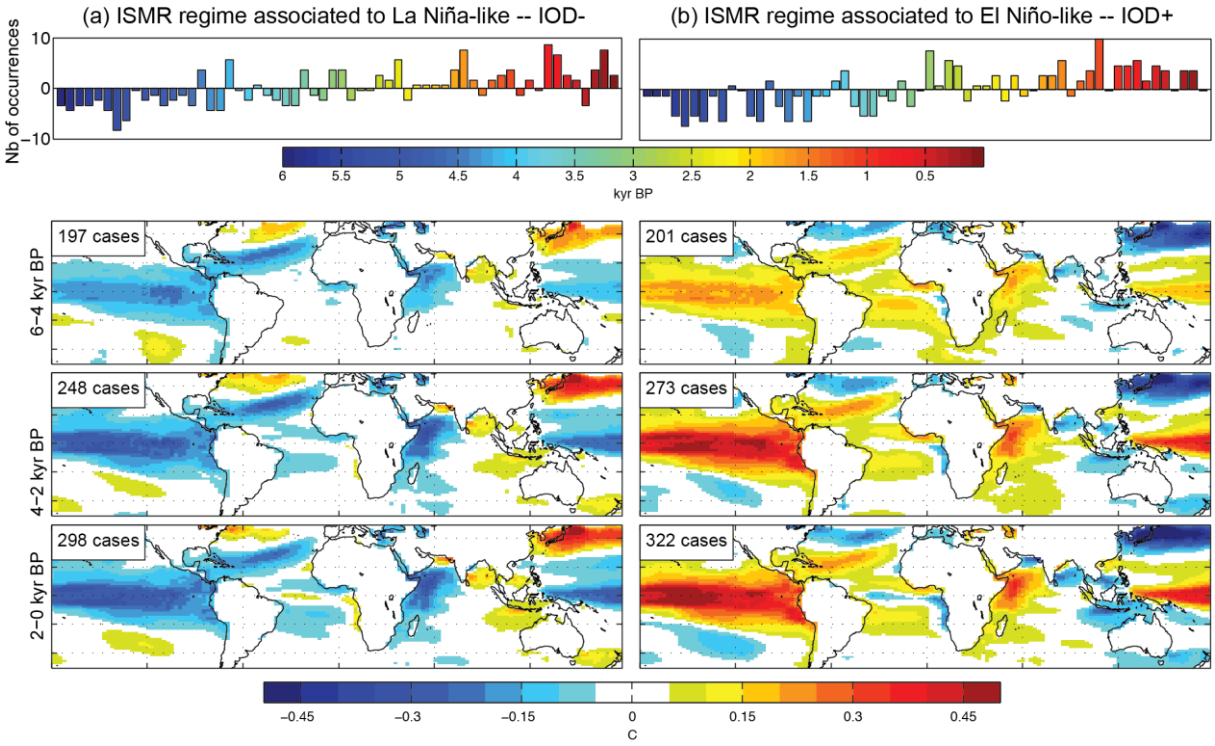

Figure 14: (a; upper panel) Century-to-century evolution in the frequency of occurrence of the ISMR regime associated to La Niña-like – IOD- collocation from 6 to 0 kyr BP for the TR6AV-Sr02 simulation. This ISMR regime is extracted by applying the AHC clustering to anomalous Indian rainfall patterns from 6 to 0 kyr BP in the two 6000-yr simulation ensemble (TR5AS-Vlr01 and TR6AV-Sr02) with a 6-regime cutoff. The frequency of occurrence is expressed as the departure from its mean value. (a; bottom panels) Number of occurrences of this ISMR regime along each 2000-yr adjacent window and associated mean anomalous SST patterns. Only SST anomalies significant at the 95% confidence level according to a Student t test are shown. (b) Same as (a) but for the ISMR regime associated to El Niño-like – IOD+ collocation.

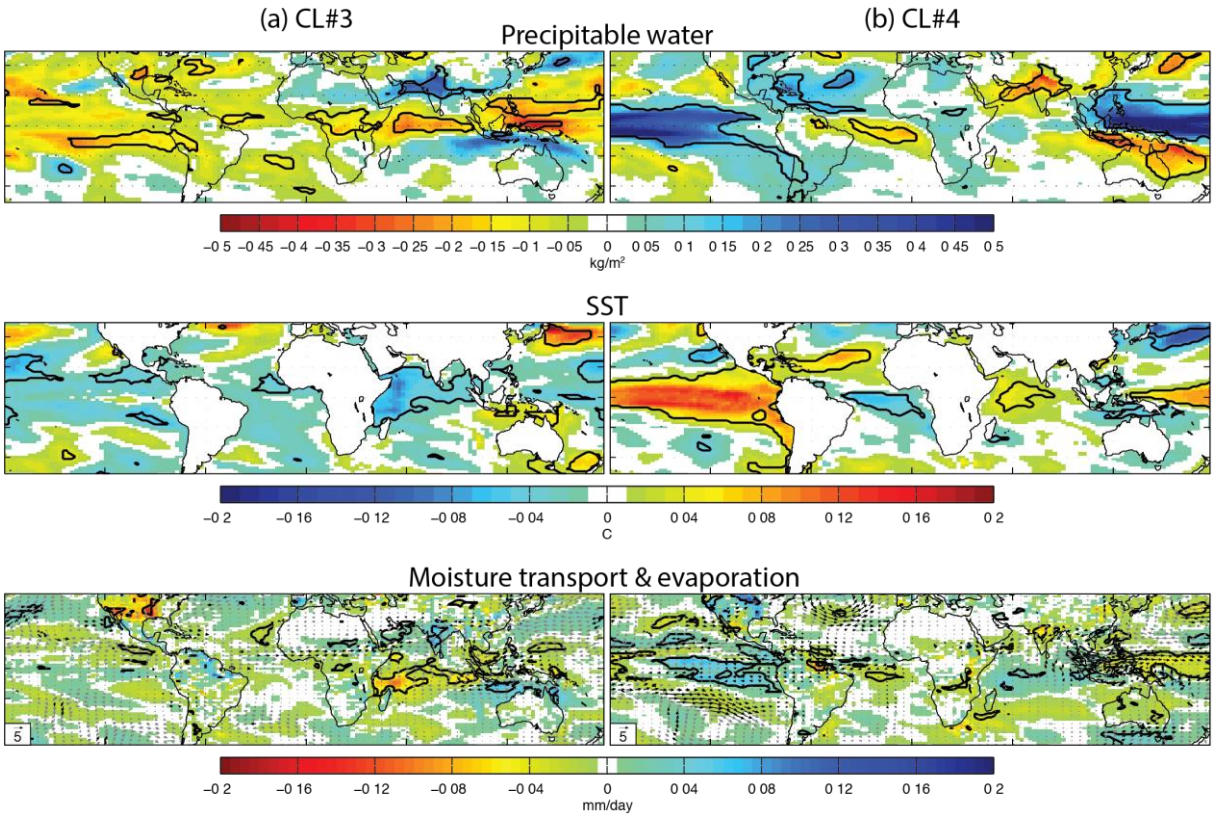

Figure 15: (a) 4.9-3.8 minus 6-4.9 kyr BP differences in precipitable water, SST, moisture transport and evaporation ensemble mean anomalies associated to regime #3. Significant anomalies at the 95% confidence level according to a Student two-tailed t test are contoured in black for precipitable water, SST and evaporation and shown with black vectors for moisture transport. (b) Same as (a) but for regime #4.

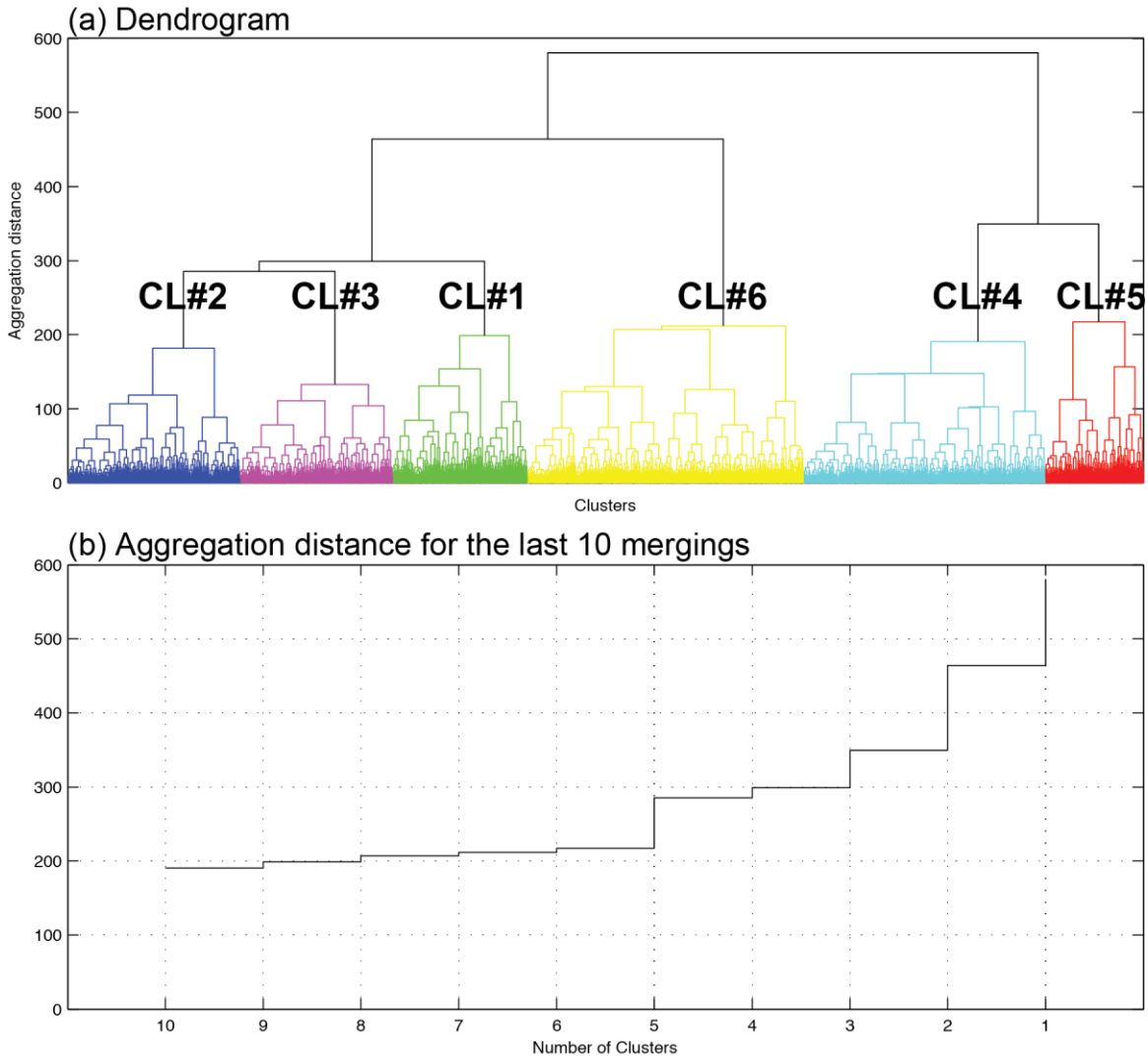

Figure A1: (a) Dendrogram tree obtained at the end of the AHC procedure applied to JJAS rainfall anomalies simulated over India by the 5-simulation ensemble from 6 to 3.8 kyr BP. (b) Evolution of the similarity metric for the 10 last mergings. See Appendix A for details.